The Astrophysical Journal, 738:167 (23pp), 2011 September 10 doi:10.1088/0004-637X/738/2/167

THE 2011 FEBRUARY 15 X2 FLARE, RIBBONS, CORONAL FRONT, AND MASS EJECTION: INTERPRETING THE THREE-DIMENSIONAL VIEWS FROM THE *SOLAR DYNAMICS OBSERVATORY* AND *STEREO* GUIDED BY MAGNETOHYDRODYNAMIC FLUX-ROPE MODELING

Carolus J. Schrijver[1], Guillaume Aulanier[2], Alan M. Title[1], Etienne Pariat[2], and Cecile Delannée[2]
[1] Lockheed Martin Advanced Technology Center, 3251 Hanover Street, Palo Alto, CA 94304, USA; schrijver@lmsal.com, title@lmsal.com
[2] LESIA, Observatoire de Paris, CNRS, UPMC, Université Paris Diderot, 5 Place Jules Janssen, 92190 Meudon, France; guillaume.aulanier@obspm.fr, etienne.pariat@obspm.fr, ceaulanier@voila.fr
Received 2011 March 23; accepted 2011 June 11; published 2011 August 23

ABSTRACT

The 2011 February 15 X2.2 flare and associated Earth-directed halo coronal mass ejection were observed in unprecedented detail with high resolution in spatial, temporal, and thermal dimensions by the Atmospheric Imaging Assembly (AIA) on the *Solar Dynamics Observatory*, as well as by instruments on the two *STEREO* spacecraft, then at near-quadrature relative to the Sun–Earth line. These observations enable us to see expanding loops from a flux-rope-like structure over the shearing polarity-inversion line between the central δ-spot groups of AR 11158, developing a propagating coronal front ("EIT wave"), and eventually forming the coronal mass ejection moving into the inner heliosphere. The observations support the interpretation that all of these features, including the "EIT wave," are signatures of an expanding volume traced by loops (much larger than the flux rope only), surrounded by a moving front rather than predominantly wave-like perturbations; this interpretation is supported by previously published MHD models for active-region and global scales. The lateral expansion of the eruption is limited to the local helmet-streamer structure and halts at the edges of a large-scale domain of connectivity (in the process exciting loop oscillations at the edge of the southern polar coronal hole). The AIA observations reveal that plasma warming occurs within the expansion front as it propagates over quiet Sun areas. This warming causes dimming in the 171 Å (Fe IX and Fe X) channel and brightening in the 193 and 211 Å (Fe XII–XIV) channels along the entire front, while there is weak 131 Å (Fe VIII and Fe XXI) emission in some directions. An analysis of the AIA response functions shows that sections of the front running over the quiet Sun are consistent with adiabatic warming; other sections may require additional heating which MHD modeling suggests could be caused by Joule dissipation. Although for the events studied here the effects of volumetric expansion are much more obvious than true wave phenomena, we discuss how different magnetic environments within and around the erupting region can lead to the signatures of either or both of these aspects.

Key words: Sun: coronal mass ejections (CMEs) – Sun: flares

Online-only material: animations, color figures

1. INTRODUCTION

Flares and coronal mass ejections (CMEs) from active regions continue to be the focus of much attention, on both the observational and theoretical-modeling fronts. These phenomena are associated with a variety of physical processes that are both drivers and consequences: flux emergence, velocity shear, the evolution of flux ropes, destabilization of magnetic configurations, and the ejection of plasma and field with attendant phenomena such as coronal propagating fronts ("EIT waves") and, ultimately, the interplanetary manifestations of the coronal mass ejection.

The initial hour or two of coronal mass ejections from active regions has been difficult to study until recently because of the relatively low cadence of full-Sun coronal imagers at quiet-coronal temperatures (such as the characteristic 15 minute cadence of the *Solar and Heliospheric Observatory*'s (*SoHO*) Extreme-ultraviolet Imaging Telescope), the limited field of view (FOV) of the high-resolution imagers (such as the 8 arcmin FOV of the high-resolution *Transition Region and Coronal Explorer, TRACE,* mission), and the inability to disambiguate the two-dimensional (2D) information for a 3D evolving transparent structure.

Since the spring of 2010, a new generation of instruments has changed our observational capabilities dramatically. The two *STEREO* spacecraft provide markedly different perspectives on solar coronal processes from what we can achieve from the Sun–Earth line. The availability of the *Solar Dynamics Observatory* (*SDO*) now enables us to view the entire visible hemisphere with unprecedented resolution in time and temperature, yet at an angular resolution in the EUV that is close to the best-ever achieved by the *TRACE* small explorer. These three state-of-the-art observatories, complemented by *SoHO*'s coronagraph, LASCO, thus provided unique observations of the first X-class flare of sunspot cycle 24, an X2.2 event starting—according to the *GOES* X-ray monitors—on 2011 February 15 01:44 UT.

This flare was associated with a pronounced halo-CME as seen from Earth's perspective provided by *SoHO*/Large Angle and Spectromeric Coronagraph Experiment (LASCO).[3] It was observed by the two *STEREO* spacecraft that were essentially in opposition, each near quadrature from the Sun–Earth line. The high cadence, resolution, and signal-to-noise ratio (S/N) of *SDO*'s Atmospheric Imaging Assembly (AIA) provided 12 s cadence observations of the flare, eruption, and beginning phases of the CME, including an outward-propagating coronal perturbation commonly referred to as an "EIT wave" after the instrument on *SoHO* with which this large-scale phenomenon was discovered (we note that they are not limited to the EUV domain; see, e.g., Hudson et al. 2003 for an example observed with an X-ray instrument).

[3] Use, e.g., Jhelioviewer to composite *SDO*/AIA images with the *SoHO*/LASCO coronagraphic observations. Web site: http://jhelioviewer.org/.

Rather than recapitulating the extensive literature on the subject of "EIT waves," or "coronal bright fronts" (CBFs) as they are also known, we summarize some key features from the extensive recent reviews by, e.g., Gallagher & Long (2010), Warmuth (2010), and Zhukov (2011), and the introductory discussion to the problem of "EIT waves" formulated by Delannée et al. (2008). Anticipating our conclusions, we suggest that neither the term "EIT wave" nor "CBF" is suitable as both the wave nature and the intensity signatures may not be consistent with these terms; instead, we use the term "coronal propagating front."

It remains a subject of debate whether the coronal propagating front is fundamentally a wave-like phenomenon or the signature of an expanding flux rope and its immediate surroundings en route to the heliosphere. The wave-like interpretation is strengthened by reports of apparent refraction and reflection of the front in regions where the Alfvén speed changes drastically (such as when the perturbation reaches either an active region or a coronal hole after propagating through quiet-Sun coronal environments), and the generally outward refraction because of the increase in the Alfvén speed with height over the photosphere (if the wave is assumed to be a fast-mode MHD magnetosonic wave). Expansion-dominated features that have been argued to have corresponding observational features are the appearance of a bright shell (adiabatically compressed and possibly heated internally by enhanced Joule dissipation) around the erupting rope, termination of the motion (sometimes described as "stationary fronts") at boundaries where the large-scale field connectivity changes drastically, changes in propagation around active regions, and the "coronal dimming"—interpreted as the result of a lowered plasma density—having a comparable extent as the CME opening angle. Part of the problem of uniquely describing an "EIT wave" as a wave or as a front lies in the ambiguity of interpreting some of the supporting attributes as caused by wave- or expansion-related phenomena, while at the same time wave and expansion signatures may often occur side by side.

In this paper, we present observations of a particularly well-observed large flare and associated halo CME from three perspectives: coronal observations from the near-Earth perspective covering a range of temperatures as recorded by *SDO*'s AIA, and from two near-quadrature perspectives with observations by the *STEREO*'s SECCHI instruments. The 12 s AIA observations show the events at a cadence that exceeds the typical *SoHO*/EIT cadence by a factor of more than 80 and *STEREO*/EUVI by a factor of over 12, have a much better angular resolution with short, high-S/N exposures, and provide a broad near-simultaneous thermal coverage. The *STEREO* observations, in turn, offer unique and critically valuable perspectives on the events observed by *SDO*/AIA on the Earth-facing hemisphere. These observations (described in Section 3) enable us to trace the evolution of the coronal emission structures from prior to the flare onset well into the heliosphere (Sections 4 and 5). We interpret these observations with the help of both global coronal potential field modeling (Section 6) and local and large-scale MHD modeling discussed in the literature (Section 7) before reaching our conclusions (Section 8).

2. A PRÉCIS OF THE CONSTRAINTS DERIVED FROM THE OBSERVATIONS

Prior to embarking on the discussion, analysis, and interpretation of the observations, we provide a summary of some of the key features in the observations, which will be important in the comparison with modeling results in later sections. We hope that placing this summary here will help the reader focus on the phenomena that we consider important for the interpretation of the events associated with the X2.2 flare and associated eruption. This section may be skipped for now and returned to prior to Section 7 for a more traditional order of presentation.

1. The eruption occurs in a quadrupolar environment. It comprises an inner bipolar δ-spot which was formed by the converging and shearing motions between the leading, respectively trailing, sunspot complexes of two bipoles emerging side by side, nearly synchronously. The trailing and leading polarities of the southern and northern bipoles, respectively, form an outer, larger-scale, bipole.
2. When the flare starts, it produces a pair of bright *J*-shaped ribbons. Each of them is located within a given polarity of the δ-spot, in the innermost dipolar cluster of the active region. Just before these ribbons start to brighten, earlier than the peak of the flare, a set of coronal loops that are tied together in the curved hook of the northeastern ribbon expand with height and apparently map down all along the straight part of the southwestern ribbon, possibly as far as along its hook. While the flare develops, secondary arc-shaped ribbons form and extend within the magnetic polarities of the outermost of the nested bipoles forming the active region.
3. Different sets of large-scale coronal loops that are rooted far from the flare ribbons are seen to expand in all directions. Even though some of them eventually slightly shrink back (or roll) toward the center of the active region, a large fraction of these loops keep expanding, apparently turning into an oval coronal propagating front, often called an "EIT wave" or "coronal bright front." Seen from the side (by *STEREO*), the expanding loops form an outward-propagating bubble, which stays rooted in the active region, and which expands and rises at least up to 100 Mm (at 1.15 $R_\odot$) above the solar surface. This expansion front, as viewed from above (*SDO*/AIA) and from the side (*STEREO A*/*B*–EUVI), propagates in projection above the solar disk, until it reaches 20° north and 32° south latitude, where it becomes unobservable from both viewpoints at coronal EUV wavelengths.
4. After an initial over-expansion of the bubble by approximately 10° both northward and southward, the coronal perturbations as seen from the side (with *STEREO A*/*B*–EUVI) relax to the same 53° range as defined by the separation of the bright stalks seen high above the limb (e.g., *STEREO*/COR2), and as defined by the latitudinal extent of the large-scale streamer-limiting field lines (potential-field source-surface, PFSS). The bright front is not seen to move beyond that (in AIA wavelengths), although some faint farther movement is seen likely much higher in the corona (*STEREO*).

3. OBSERVATIONS

For the present study, we use observations from the AIA on NASA's *SDO* (Lemen et al. 2010). The instrument was taking exposures in sets of four every 6 s, cycling through a full set of eight every 12 s. The EUV exposures in each channel were taken alternatively with fixed exposure times and subject to automatic exposure control (AEC). The AEC can step the exposures down from the standard 2.0–3.0 s for most of the coronal EUV channels to as low as 0.05 s to prevent very bright sources from saturating the images too much. Thus, EUV image

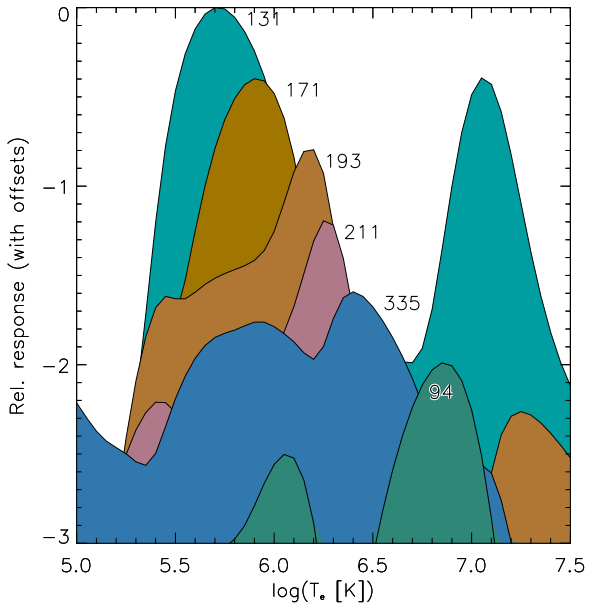

Figure 1. Peak-normalized response curves (for the instrument response in DN/pixel/s) for the *SDO*/AIA instrument, downward offset by powers of 2.5 in this order: 131, 171, 193, 211, 335, and 94 Å. The areas are shaded with the color characteristic of the standard AIA color tables (as used in online Movie 2).

(A color version of this figure is available in the online journal.)

sets were obtained with 12 s cadence for the following channels: set I with 304 Å (He II), 211 Å (Fe XIV), 335 Å (Fe XIV), and a UV exposure alternating in the 1600 Å and 1700 Å channels, and set II with 94 Å (Fe XVIII), 171 Å (Fe IX), 193 Å (Fe XII and Fe XXIV), and 131 Å (Fe VIII and Fe XXI). Each set has exposures starting simultaneously, but ending differently as set by the exposure time. All AIA exposures are normalized by exposure time; for running-difference images we use only images with the same, fixed, exposure time to avoid changes in S/N and detector backgrounds.

The ion spectra listed above are those generally dominant in the channels, but other ions and their continua can also contribute. The relative shapes of the response curves for the coronal EUV channels of *SDO*'s AIA (see Boerner et al. 2011) are shown in Figure 1; note that these curves are offset by an increasing multiplicative factor to enable us to show the locations of the main peaks in the response curves. Note that several of the channels have dual peaks; the 171 Å and 193 Å channels stand out in that their secondary peaks are markedly lower than their primary peaks so that the interpretation of the signal is less ambiguous. In general, we compare multiple channels to reach conclusions regarding a thermal structure along a line of sight (LOS).

Line-of-sight magnetograms were obtained by the Helioseismic and Magnetic Imager (HMI; Schou et al. 2011) on a 45 s cadence.

The two *STEREO* spacecraft provided near-quadrature observations of the solar corona and inner heliosphere with the SECCHI EUVI and coronagraph imagers, COR1 and COR2 (Howard et al. 2008). At the time of the flare, *STEREO A* was 86.°8 ahead of the Sun–Earth line and *STEREO B* 94.°1 behind (with a separation between them of 180.°9, i.e., in near-perfect opposition). SECCHI/EUVI 195 Å data are available at 2.5–5 minute cadence and the COR1, 2 data at 10 minute cadence.

4. ACTIVE-REGION CORE AND FLARE ONSET

The entire emergence phase of AR 11158 was observed by HMI in the days prior to the X2.2 flare (see Movie 1). Two bipolar regions began this emergence in close proximity, with the trailing polarity of the northern bipole subsequently colliding with and then sliding along the leading polarity of the southern bipole (Figure 2). The interface between these patches of strong field regions, in which multiple penumbrae of both polarities were enveloped in a continuous wreath of penumbral fields (thus forming a complex δ spot group), formed a high-gradient, strong-field interface with pronounced velocity shear along which large flares frequently are seen to initiate (see the review by Schrijver 2009). Figure 3 shows this polarity pattern in the lower-right panel at 2011 February 15 01:47 UT, near the start time of the X2.2 *GOES* flare.

The X2.2 flare[4] and eruption of 2011 February 15 in AR 11158 (class $\beta\gamma$) started in the *GOES* X-ray signal at 01:44 UT, with a peak X-ray flux at 01:56 UT. At the time of the flare, AR 11158 was located at (S21, W21); see Figures 4 and 5. Online Movie 2 shows the flare, eruption, and expanding coronal perturbation front in the *SDO*'s AIA 211 Å channel from just prior to the expansion phase of the loops to past the peak of the X-ray flare; select sample images are shown in Figure 6. Table 1 summarizes some phases in the early flare development.

The first signs of activity within the very core of AR 11158 from where the most prominent flux rope is ejected are seen at 01:45 UT as brightenings on the flare ribbons, which brighten rapidly over the next few minutes (see online Movie 3 and the running-difference Movies 5–7). The first diffraction patterns (induced primarily by the supporting grids on the thin filters at

[4] SOL2011-02-15T01:46:50L033C108.

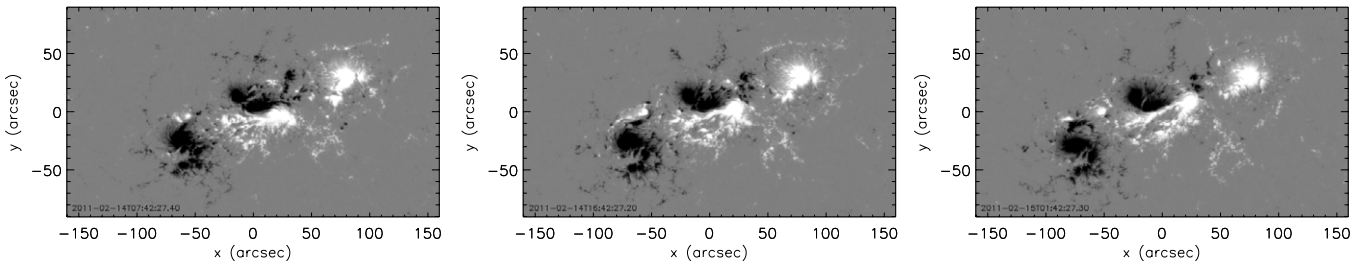

Figure 2. Sample HMI magnetograms of AR 11158 16, 8, and 0 h before the start of the X2.2 flare. The intensity scale saturates at ±1500 Mx cm^{-2}. Movie 1 shows the evolution of the region over a 5D interval prior to and just after the flare. Compare with Figure 3 and Movie 3 for alignment of the magnetogram with the overlying coronal features. Movie 1 shows the HMI magnetogram sequence (640 × 360 pixels of 0.50 arcsec each) tracing the emergence and evolution of AR 11158 from 2011 February 10 14 UT to 2011 February 15 06 UT. The scale saturates at ±1500 Mx cm^{-2}.

(An animation (Movie 1) of this figure is available in the online journal.)

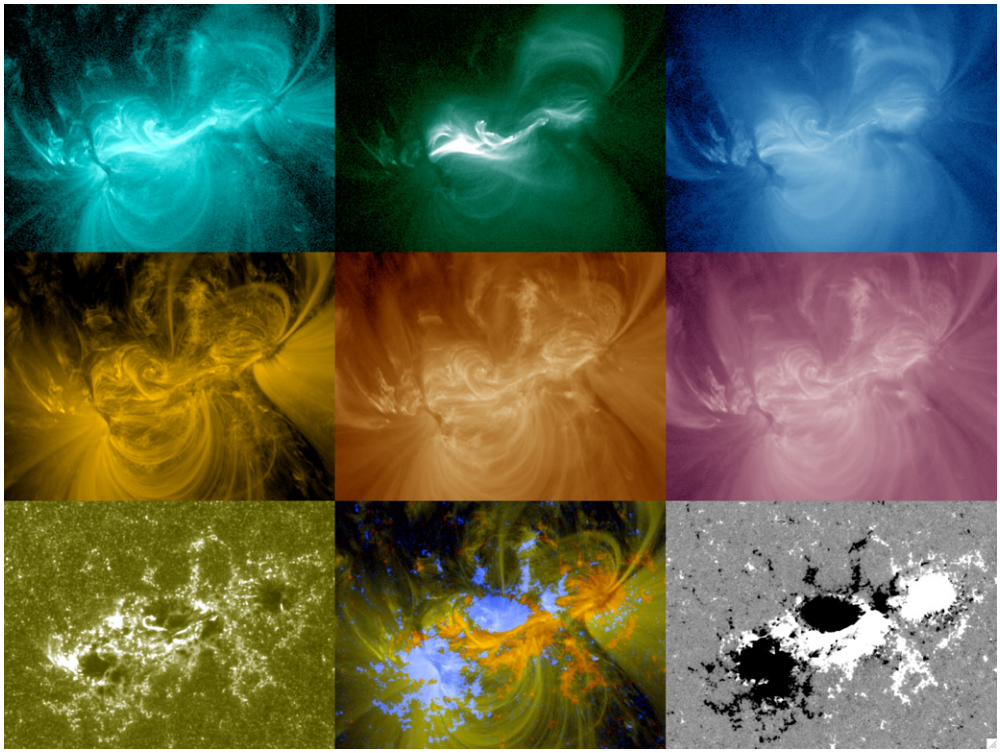

Figure 3. Composite of AIA images and (lower-right) an HMI magnetogram, all taken within 13 s from 2011 February 15 01:46:56 UT. Top row: the channels sensitive to high temperatures: 131, 94, and 335 Å. Center row: the channels sensitive to ∼1–2 MK: 171, 193, and 211 Å. Bottom row: comparisons with lower atmosphere: 1600 Å channel, a blend of the 171 Å image with a line-of-sight magnetogram, and the HMI LOS magnetogram. The field of view of each panel extends over 480 pixels in the east–west direction or 210 Mm. Movie 3 shows the image sequence of composites of AIA images and (lower-right) an HMI magnetogram, showing frames at a 12 s cadence (and the nearest available HMI LOS magnetogram) starting at 2011 February 15 01:45:00 UT. Top row: an RGB blend of 94, 335, and 193 Å images next to the channels separately which are sensitive to relatively high temperatures (see Figure 1 for a comparison of response curves): 131, 94, and 335 Å. Center row: the channels sensitive to ∼1–2 MK: 171, 193, and 211 Å, with the leftmost panel showing these as an RGB blend. Bottom row: comparisons with lower atmosphere: 304 and 1600 Å channels, a blend of the 171 Å image with an LOS magnetogram and the HMI LOS magnetogram. The FOV of each panel extends over 480 pixels in the east–west direction, or 210 Mm. The movie covers the time interval from 01:45 UT to 02:45 UT (compare with the 335 Å light curve in Figure 7).

(A color version and an animation (Movie 3) of this figure are available in the online journal.)

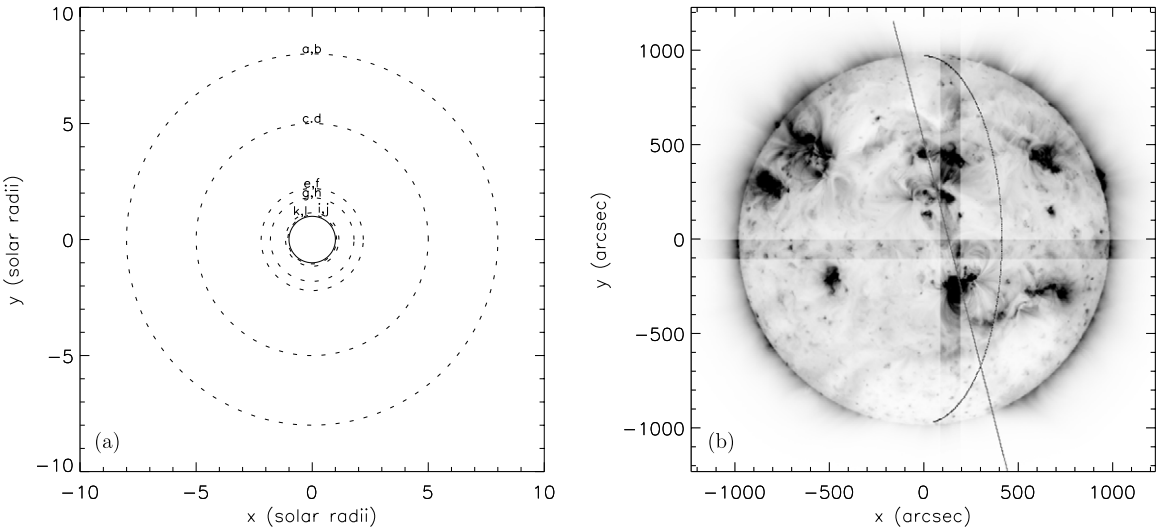

Figure 4. (a) Illustration of the distances at which the signals were measured for Figure 16, labeled with the panel identifications. (b) Sample (negative) AIA 193 Å image showing the great circle at which the intensities were measured for Figure 16(n) at 25° west of central meridian, the linear cut used to measure intensities shown in Figure 8, and (with enhanced contrasts) the horizontal and vertical slices used for Figure 12.

the front ends of the telescopes) become clearly visible between 01:47 UT and 01:48 UT, reflecting very concentrated bright structures. At that time, the flare is strong enough to cause a rapid increase in the solar spectral irradiance in all channels; an example of that for the AIA's 335 Å channel is shown in Figure 7. The *GOES* brightness continues to increase to the X2.2 level at 01:56 UT; the 335 Å light curve in Figure 7 also shows this rapid increase, after which the increase slows and becomes irregular (affected in the details of the light curve by the detector saturation on the brightest regions of the flare, which is reflected in the alternating high and low signals for the short and long exposures once the AIA's AEC algorithm is activated).

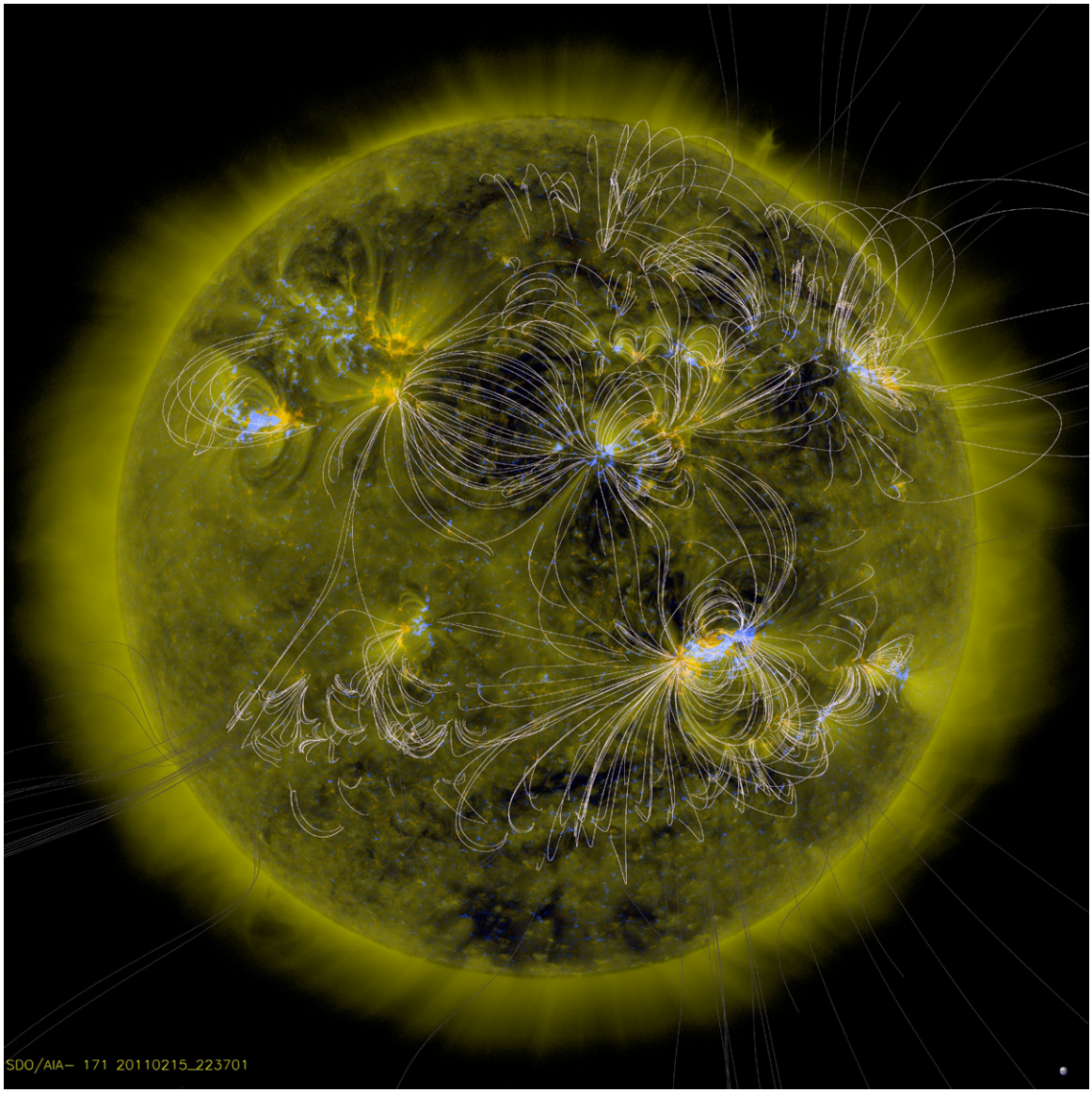

Figure 5. Potential-field source surface field lines shown projected onto an *SDO*/AIA 171 Å image taken on 2011 February 15.
(A color version of this figure is available in the online journal.)

Table 1
Phases in the Early Flare Development

Time (UT)	Note
01:44	*GOES* flare start.
01:45	Flare ribbons initiate. First loop expansion.
01:47–48	*J*-shaped ribbons form and brighten. Loop expansion accelerates.
01:48:18	Flare ribbons extend beyond central δ spot.
01:50:15	Ribbons reach into leading spot.
01:50–53	Expanding loops fade.
01:53–54	Expanding coronal front forms.
01:56	*GOES* flare peak. Ribbons reach maximum extent.

Prior to about 01:48:18 UT, the flare ribbons are confined to the central spot composite. A pronounced *J*-shaped hook is persistently visible on the eastern, trailing side. A more compact *J*-shaped hook is partly outlined from the start of the flare, but becomes fully outlined at about 01:49:03 UT. After about 01:48:18 UT, flare ribbons are also seen ending on the trailing umbra and from about 01:50:15 UT onward also in the umbra of the leading spot. The ribbons appear to reach their maximum geometrical extent by about 01:56 UT, just when the *GOES* X-ray flux peaks. We note that Kosovichev (2011) reports on a helioseismic sun-quake associated with the initial eastern flare ribbon, apparently excited around 01:51 UT.

We interpret the compact pair of *J*-shaped ribbons (see Section 7.1.2) as the bounding footprint of the outer perimeter of an erupting flux rope (showing no signs, by the way, of dark prominence material in the He II 304 Å channel, compare Movie 3). The outer set of flare ribbons likely reflects interaction of the destabilizing rope with higher field patterns in the predominantly quadrupolar configuration of AR 11158. We return to this interpretation in Section 7.

From 01:45 UT onward, the very beginning of the flare, there are signs of expanding bright structures, likely coronal loops, away from the primary polarity inversion line in all of AIA's coronal channels. The displacement velocity of these loops accelerates rapidly just after 01:47 UT. To quantify these displacements over time, we determine the intensity profile

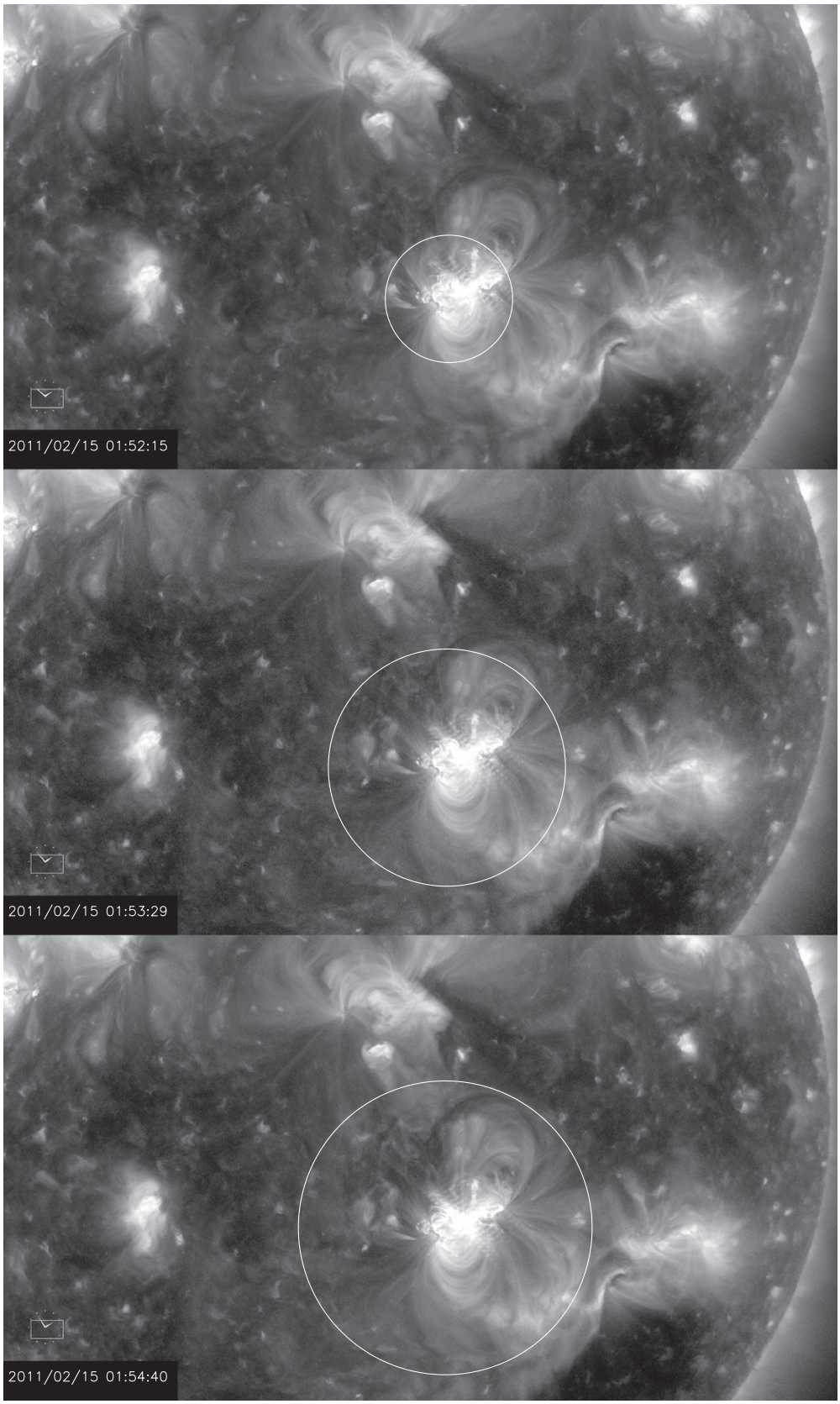

Figure 6. Composite of three *SDO*/AIA frames taken in the 211 Å channel. Circles outline approximately the envelope of the expanding loops (top) transitioning into an expanding front (bottom), not reflecting the anisotropy of this expansion. The field of view is shown as a rectangle on the clock face, with that face representing the solar disk. See Movie 1 for all 211 Å exposures taken between 01:46 UT and 02:08 UT on 2011 February 15. Movie 2 shows the image sequence in the *SDO*/AIA 211 Å channel showing the flaring region AR 11158, the expanding loops from its core, and the propagation of the coronal perturbation front associated with it. The movie runs from 01:46 UT to 02:08 UT on 2011 February 15.

(An animation (Movie 2) of this figure is available in the online journal.)

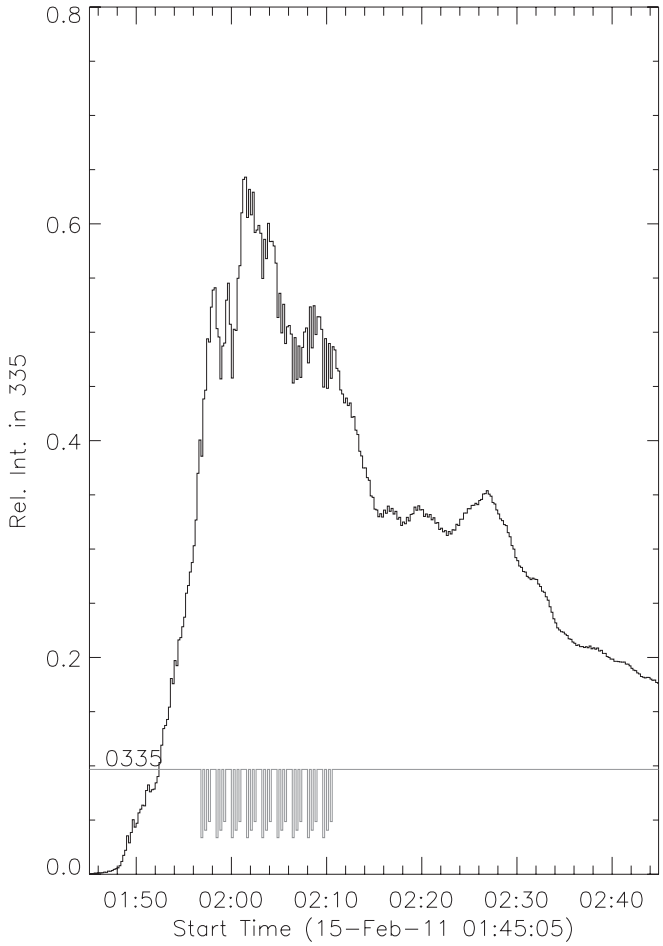

Figure 7. Light curve for the full-Sun signal in the *SDO*/AIA 335 Å channel, showing the relative intensity normalized to the *GOES* flare-start time at 2011 February 15 01:45 UT. The gray histogram shows the exposure times, scaled down by a factor of 30, to show the action of the automatic exposure control system.

along a cut across the AIA images. The track, shown in Figure 4(b), cuts across the center of the primary polarity-inversion line of AR 11158 at a slight angle relative to the N-S direction in order to lie between the main areas of detector saturation and the most pronounced diffraction patterns. We integrate the signal over 5 pixels (0.6 arcsec each) in the east–west direction from the track to increase the S/N; this slanted track is displaced by an integer number of pixels to compensate for solar rotation.

Running-difference stack plots for the intensity profiles along the slanted track centered on AR 11158 are shown in Figure 8 (in the order of the top two rows of panels in Figure 3 plus 304 Å). Near the center of the frames, the images are saturated because of the bright flare, compounded by the bleeding of electrons on the CCDs primarily in the north–south direction; alternating short and longer exposures lead to black-and-white ridge pairs near this central frequently saturated region. The mostly saturated-white features on the southern (negative y) side of the flare site seen in 304, 171, 193, and 131 Å are image artifacts associated with CCD supersaturation and ensuing electron bleed.

The displacement velocity along the most prominent feature marked by the white line in Figure 8 (observed most readily in the 335 Å channel) increases smoothly from $\sim$170 km s^{-1} at the start to $\sim$450 km s^{-1} at 01:53:30 UT. If the path of the feature is approximated by an exponential, the characteristic e-folding timescale is found to be 5.1 minutes in this time range. Figure 9 shows this track on a log-log scale, discussed further below.

Some other features stand out in the time slices. Figures 8(b) and (c) (94 and 335 Å) show inward-moving ridges on the southern side of the region, apparently starting on the ridge of the outward-moving structure. These appear to be the counterparts of loop-like features seen moving toward the polarity-inversion line in AR 11158. These may be low-lying loops moving into the volume left behind by the rising flux rope, or part of the flux rope as it spins while rising. We return to this in Section 7. More of such inward-moving structures are seen in Figures 8(d)–(f) further away from the polarity-inversion line; these features are more readily matched to inward-moving quiescent and relatively cool loops.

5. CORONA TO HELIOSPHERE: OBSERVATIONS

5.1. On-disk Signatures

On scales large compared to those of the active regions, the high-cadence, high-S/N *SDO*/AIA observations show a wave-like front propagating away from the flare and eruption site. The coronal bright front, particularly well visible in the AIA 193 Å channel, propagates in all directions from the flare site (see online Movie 4). Its propagation toward the south and southwest continues until it reaches the edge of the coronal hole at which point the brightness perturbation vanishes. As it hits the interface between quiet-Sun and coronal hole, the coronal brightness patterns exhibit an oscillatory motion. In the *STEREO*/EUVI 193 Å images (taken at a much lower cadence), these perturbations appear to occur only in the high corona, some 100 Mm or more above the surface (see online Movie 4). Toward the east, northeast, and north, the coronal bright front travels substantially farther, out to some 50°–60° east, and reaching clearly up to about 22°N in the EUV observations.

The running-difference images in Movie 6 show the front clearly propagating outward at first as described above. Then, as the propagation of the primary signature stalls (for which we discuss our interpretation below), very faint intensity perturbations continue beyond that in certain areas, no longer quasi-radial from the flare site. These are so weak that they cannot be unambiguously traced. Some of these extend outward off the solar disk, reaching into the noise at the edges of the AIA field of view. Faint signatures of perturbations are seen running out in the *STEREO* EUVI images in Movie 4 almost to the disk centers from their respective perspectives, i.e., reaching to nearly the limb seen from *SDO*; specifically, they reach a Carrington longitude of approximately $\sim-60°$ at about 03:00 UT for *STEREO B* and $\sim+105°$ at about 02:35 UT in *STEREO A*; their average propagation speed from the onset of the expansion at 01:47 UT is thus about 80 ± 10 deg hr^{-1} and 100 ± 10 deg hr^{-1}, respectively (or 270 ± 35 km s^{-1} and 340 ± 35 km s^{-1} if we assume this to propagate over the solar surface, which is an underestimate; see Section 5.2). We discuss this feature further in Section 5.2 as we describe a faint extension northward that is visible in COR1 to even reach the north polar region beyond 0.8 solar radii above the surface.

Inspection of the AIA image sequences reveals the signature of the coronal bright front that is seen most clearly in 193 Å to be very faint in 304 Å only toward the north, while in 94 Å the diffracted and scattered light from the bright flare region outshines any signal change associated with the front. In 131 Å, a very weak signature of the front is seen moving toward the north and south, but not over the quiet Sun toward the east or

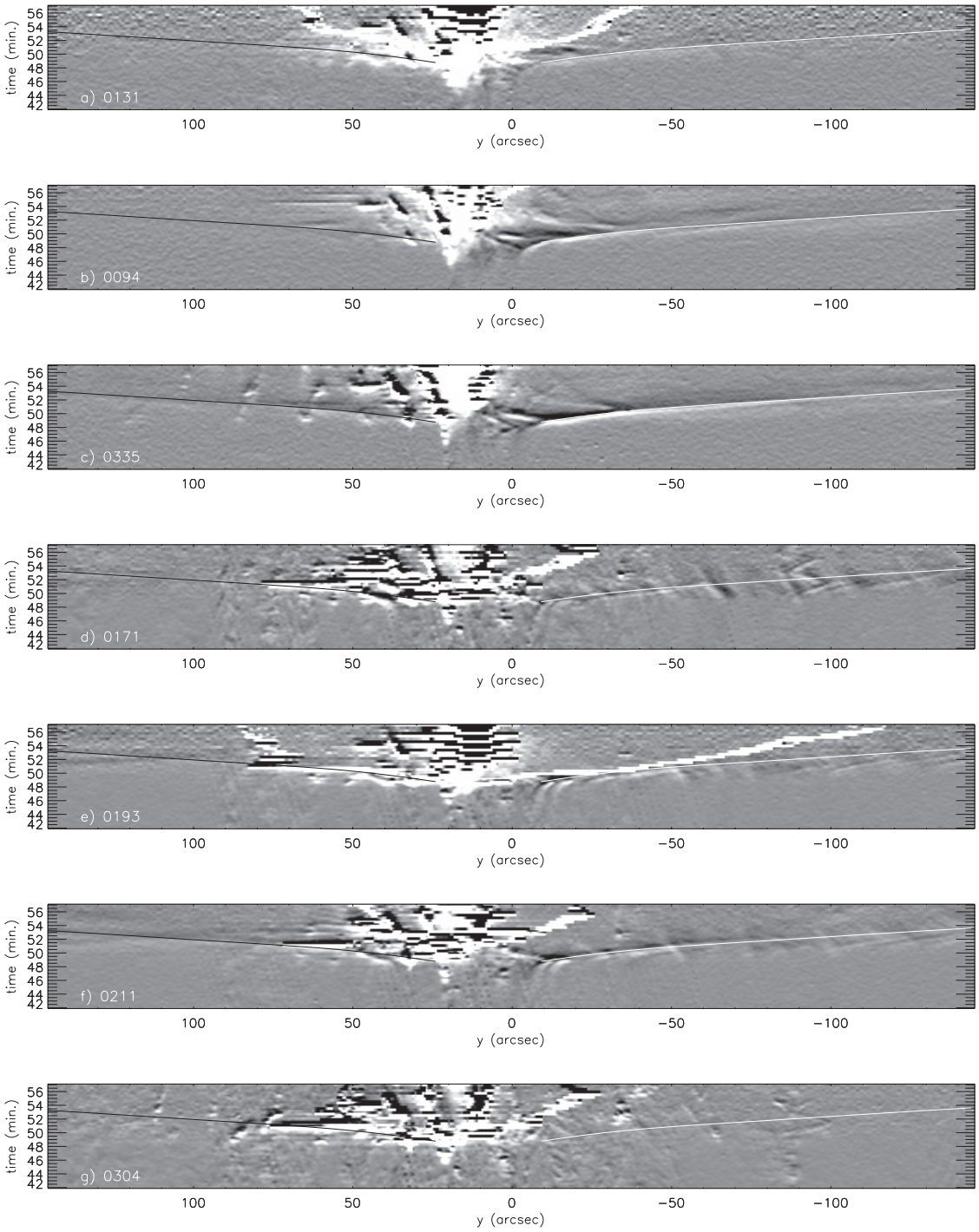

Figure 8. Time slices for running differences in all seven AIA EUV channels (image pairs were used with a temporal spacing of 96 s). The slices follow the slightly inclined track indicated by the gray straight line in the right panel of Figure 4. The white curve in each panel follows the track of an outstanding feature running southward (toward higher negative coordinate values) in the 335 Å channel, repeated in each panel; the black curve is a mirrored track shifted to match a northward-moving feature in the 335 Å channel. The displacement velocity along the cut increases gradually from ∼170 km s^{-1} at the start, continuing a smooth increase to 450 km s^{-1} at the edge of the panels.

west. The front is clearly seen at channels most sensitive to the temperatures of the quiet-Sun corona: 171, 193, 211, and 335 Å. In 335 Å the front is readily seen in the northward and southward directions, but appears absent due eastward and westward. In 171 Å the front is predominantly a dimming, whereas in 193 and 211 Å, a brightening precedes a subsequent dimming (see the sample images and running-difference images in Figure 10 (and the associated color scale in Figure 11) and online Movies 5–7).

As noted in earlier studies for other fronts (e.g., Delannée et al. 2008), the 2011 February 15 front expands anisotropically while it is also far from uniform in strength in different directions. The running-difference images in the second and fourth columns of Figure 10 show a front most clearly at directions from SE via N to NW, but even within that arc there are differences in the various directions (see Movies 5–7).

Figure 12 shows snapshot examples of the intensity profile of the coronal front, expressed as a relative change in intensity,

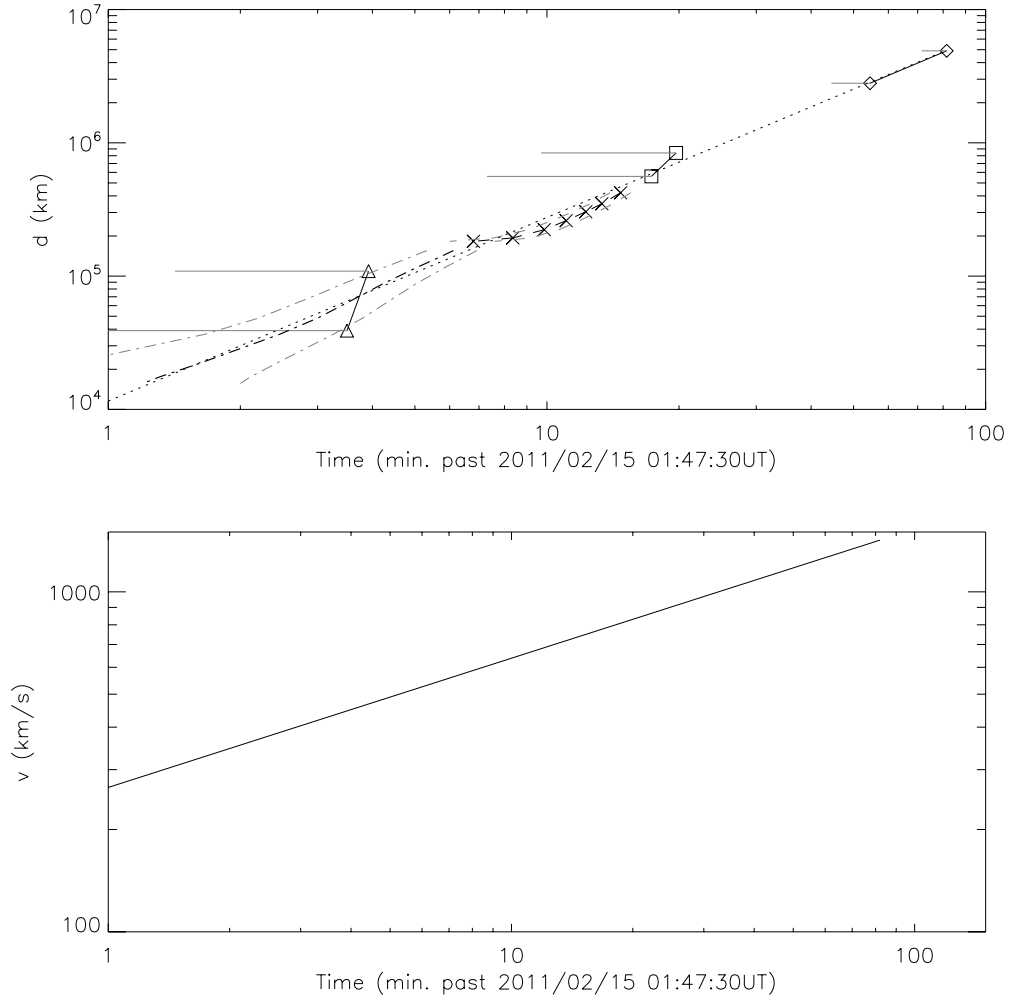

Figure 9. Top: expansion of the loops, front, and CME. For radial displacements: diamonds: *STEREO A*/COR2; squares: *STEREO A*/COR1; triangles: *STEREO A*/EUVI/195. For displacements measured on disk: crosses: expansion front for AIA 193 Å at the central meridian (measured along a great circle through the central flare site); dash-dotted line: expansion feature traced in AIA 335 Å (Figure 8), assuming a 45° inclination relative to the local horizontal direction of the loops that are being tracked. Gray bars indicate uncertainties: for the *STEREO* data, these show the time difference between the image in which a feature is first seen and the preceding image, for AIA data these are estimated uncertainties based on the approximations to the ridges seen in Figures 8 and 16(m). The dotted line is a power law with exponent 1.38 (Equation (5)). Bottom: velocity as the derivative of the power-law fit to the observed displacements in the top panel.

i.e., the signal $r(x)$ shown is defined as $r(x) = 2(r(x, t_1) - r(x, t_0))/(r(x, t_1) + r(x, t_0))$. The panels show relative intensity profiles for 211, 193, 171, and 131 Å for the east–west and north–south cuts (as shown in Figure 4). The east–west cut (left) runs across the quiet Sun only, while the north–south cut (right) runs across several regions of enhanced magnetic activity and the interconnections between them.

For the quiet-corona profiles in 211 and 193 Å (top two panels on the left), coronal bright fronts are readily recognized around $x = -200$ and +450. The eastward-propagating front shows no clear response at its leading edge in 171 Å and a dimming toward the trailing edge on the side facing the flare. The westward-propagating front shows only a very faint brightening in 171 Å. The 131 Å signals (bottom panels) appear to be dominated by the profile of the scattered and diffracted light from the bright flare kernel.

For the north–south profiles, the front stands out in 211 Å, is essentially absent in 193 Å, and exhibits a dimming in 171 Å (consistent with the running-difference Movies 5–7). The 131 Å signal is very weak: a visual inspection of Movie 7 shows a faint brightening, but that is close to the noise and hard to separate unambiguously from the pedestal formed by scattered and diffracted light as seen in the intensity profile in Figure 12.

The relative changes in the quiet-corona (east–west) intensity profiles suggest that the fronts are not only brightenings but also correspond to warmings, causing the 171 Å signal at the trailing end of the fronts to correspond to dimmings even as these are brightenings in 211 and 193 Å; the warming trend extends over the approximately 3 minutes that it takes for the front (with half-width of ∼150 arcsec moving at about 600 km s^{-1}) to travel over its own width. The changes for the north–south cut are more difficult to interpret—we return to that below.

These base-difference light curves based on observations with high resolution in both space and time clearly demonstrate that the propagating coronal front studied here is not the same in strength or structure at different wavelengths, and differs in different directions along the front. At least over the quiet corona, the light curves suggest that we are not looking at an isothermal compression front, but rather at a front in which the temperature increases from front to back (compare Wills-Davey & Thompson 1999); there may be a compressional component, but the general dimming character of the front segments seen in 171 Å suggests that there is at least a warming which the compression does not compensate for. We can study this more quantitatively using the AIA instrument response curves.

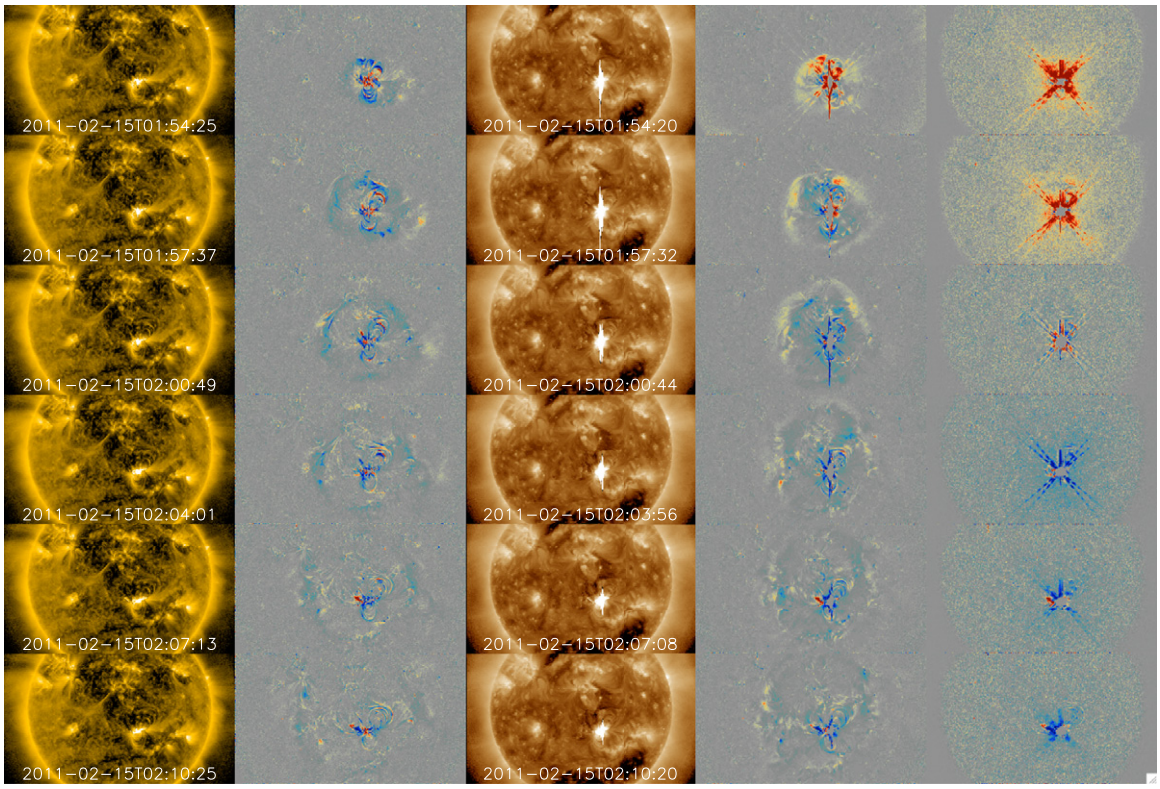

Figure 10. Composite of images in AIA's 171 and 193 Å channels (Columns 1 and 3) and the associated running difference images (Columns 2 and 4; compare Movies 4 and 5), and the running difference images in the 131 Å channel (Column 5; compare Movie 6). The running difference images (based on a temporal spacing of 96 s) are displayed as yellow to red for increasing brightening, and as light blue to dark blue for increasingly strong dimmings (see Figure 11). Movies 5, 6, and 7 show running difference movies for AIA's 171 Å, 193 Å, and 131 Å, channels, respectively for 2011 February 15 00-03 UT. Yellow to red indicate increasingly strong brightenings, light blue to dark blue increasingly strong dimmings. The images were smoothed over 3 pixels to reduce the noise and image pairs were used with a temporal spacing of 96 s; absolute difference can be estimated using Figure 11 with a multiplier of 11, 8.5, and 1.1 DN s^{-1} in movies 5, 6, and 7, respectively. Each image shows the full width of the AIA FOV (40 arcmin). Time stamps for $I_{i+1} - I_i$ show times i.

(Animations (Movie 5, Movie 6, Movie 7) of this figure are available in the online journal.)

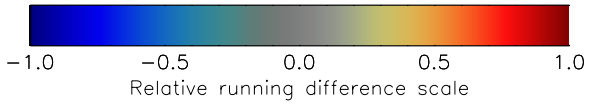

Figure 11. Color scaling for the running difference Movies 4–6 and the running-difference images (Columns 2, 4, and 5) in Figure 10. The scale should be multiplied by 11, 8.5, and 1.1, respectively, for 171, 193, and 131 Å to obtain changes in DN s^{-1} between image pairs.

If we assume that the change in the signals $\partial I_{171,193,211}/\partial t$ are caused by changes in the emission measure E_f and temperature T_f of the high coronal plasma, then these changes can be written, for wavelength i and AIA response functions $R_i(T_f)$ that define the observed intensity $I_i = R_i(T_f)E_f$, as

$$\frac{\partial I_i}{\partial t} = \frac{dR_i(T_f)}{dT_f}\frac{dT_f}{dt}E_f + R_i(T_f)\frac{dE_f}{dt}. \quad (1)$$

For $\partial I_{171}/\partial t$ to be negative and $\partial I_{193,211}/\partial t$ to be positive, for example, as we see for the inner edges of the fronts toward the east and west:

$$-\frac{d\ln(R_{171})}{d\ln(T)} > \frac{d\ln(E_f)}{d\ln(T)}, \quad -\frac{d\ln(R_{193,211})}{d\ln(T)} < \frac{d\ln(E_f)}{d\ln(T)}. \quad (2)$$

Let us assume a purely adiabatic and uniform compression of a slab of plasma that is wider than the image resolution, aligned with the LOS, and compressed perpendicular to it. For adiabatic compression $TV^{\gamma-1}$ is a constant, with temperature T and volume V and adiabatic index $\gamma = 5/3$. In this configuration, the plasma density n scales with volume V as $n \propto 1/V$. Given that emission measure E scales as $E \propto n^2$, one can derive that

$$\frac{d\ln(E_f)}{d\ln(T)} = 3. \quad (3)$$

Figure 13 shows that the inequalities in Equation (2) are met for plasma within the characteristic thermal range of the high quiet corona between ~1.2 MK and ~1.8 MK. Our inference that the coronal expanding front is associated with a warming is therefore at least qualitatively compatible with the trends expected for adiabatic compression of a plasma just below 1.1 MK in the east and just above that in the west.

If we assume that adiabatic compression is the only reason for the plasma warming, then Equation (1) can be rewritten to read

$$-\Delta\ln(E_f) = \left(\frac{1}{3}\frac{d\ln(R_i(T_f))}{d\ln(T_f)} + 1\right)/\Delta\ln(I_i). \quad (4)$$

This expression can be used in combination with the observed relative intensity changes to estimate temperatures, assuming (approximately) isothermal plasmas: for observations consistent with the adiabatic assumption, the above expression should yield the same value for all wavelengths for which the contrast in the front can be provided. The observed contrasts are listed in Table 2. Figure 14 shows that the fronts that propagate over a purely quiet Sun are consistent with adiabatic compression

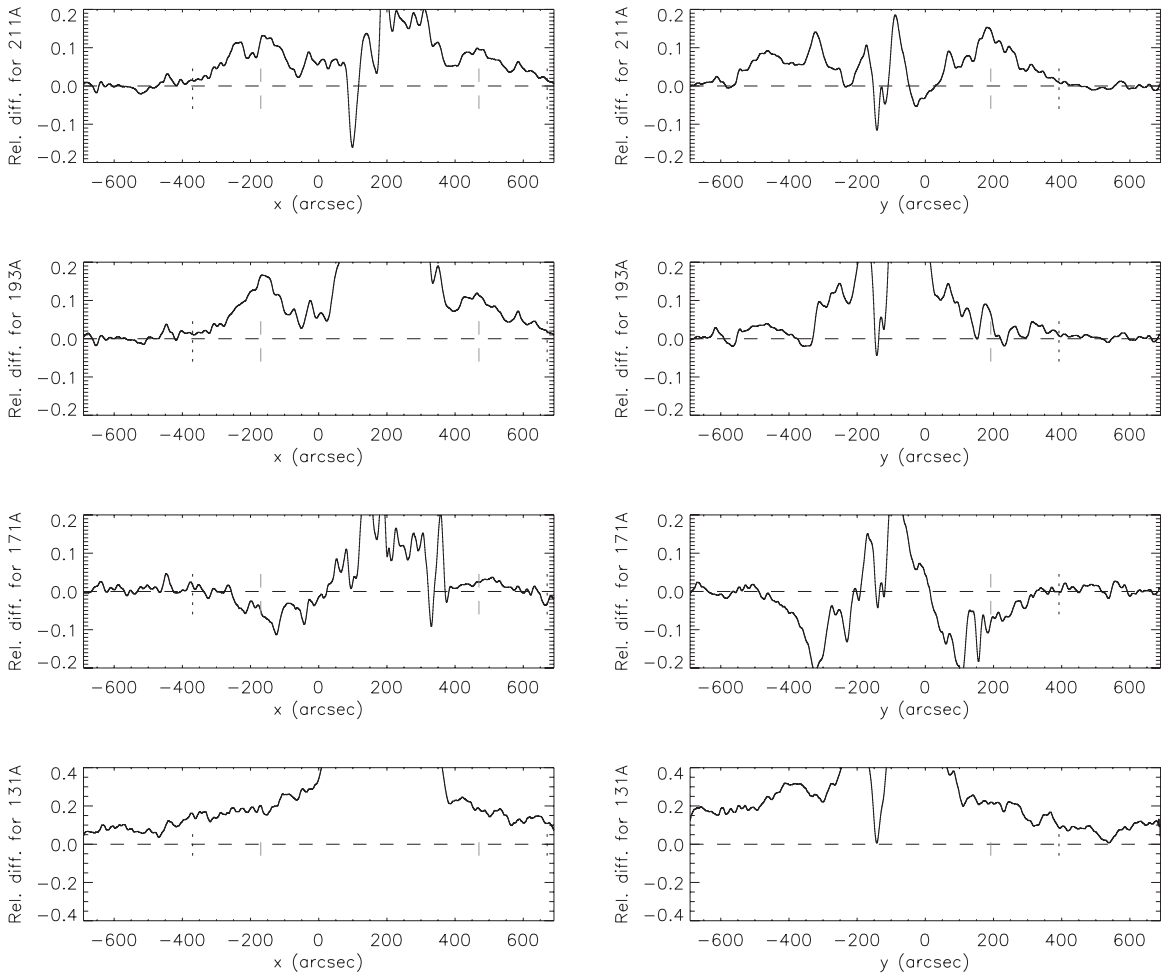

Figure 12. Relative intensity changes for strips of 100 arcsec width running east–west (left) or north–south (right) as shown in Figure 4 for *SDO*/AIA images in 211, 193, 171, and 131 Å, respectively, taken at 01:58:20 UT and 01:47:56 UT. $(x, y) = (0, 0)$ corresponds to disk center. Positive change denotes a brightening; a smoothing over 12 arcsec has been applied. Vertical dotted and dashed lines indicate the approximate leading edges and peaks, respectively, in the propagating coronal fronts.

Table 2
Intensity Ratios for the Three Coronal Propagating Fronts Identified in Figure 12 (and the Line Types Used in Figure 14) for a ≈50 arcsec Window around the Positions Marked by the Vertical Dashed Line Segments in Figure 12, Giving the Ratio of Intensities between the Peak of the Front Observed at 01:58:20 UT and the Pre-event Intensity at 01:47:56 UT

Channel	Line type	Eastern $x \approx -200$	Western $x \approx 450$	Northern $y \approx 200$
171 Å	Dotted	-0.05 ± 0.02	-0.02 ± 0.01	-0.05 ± 0.02
193 Å	Solid	$+0.13 \pm 0.03$	$+0.10 \pm 0.02$	$+0.02 \pm 0.02$
211 Å	Dashed	$+0.09 \pm 0.02$	$+0.09 \pm 0.02$	$+0.12 \pm 0.02$
131 Å	Dash-dotted	...	...	$+0.20 \pm 0.05$

for a temperature of 1.30 ± 0.03 MK in the eastern front and 1.3 ± 0.1 MK in the western front (the uncertainty ranges are lower limits as we have not considered uncertainties on the response curves). Marginal solutions for these two fronts also exist at 2.5 MK. As the solutions for ≈1.3 MK are consistent with those characteristic of the high quiet-Sun corona, we suggest that these are the likely values. Using Equation (4), we estimate a maximum density increase of ≈10% in the eastward- and westward-propagating fronts, associated with a temperature increase of ≈7% (Equation (3)).

For the northward-propagating front we find no consistent solution for the four channels. Figure 12 illustrates that it is difficult to unambiguously separate a 131 Å front from the scattered/diffracted light, but we do see a faint northward-propagating brightening in the running-difference Movie 7. For the estimated contrast range in 131 Å, there is no solution consistent with the isothermal and adiabatic assumption. Hence, for this front we should allow for some heating in addition to the anticipated adiabatic warming, while remaining aware of uncertainties in the AIA response curves which are not considered here and of the limitations of the assumption that the plasma is isothermal and uniformly compressed along the LOS.

5.2. Off-disk Signatures

The *STEREO* instruments enable us to track the CME outward from the surface. Sample images for the COR2 instrument on *STEREO A* are shown in Figure 15, and in online Movies 8 and 9 for *STEREO A* and *B*, respectively. A visualization of the development of the CME as it bulges out and away from the flare site is shown in Figure 16, which contains panels derived from observations from *STEREO Behind* (left column) and *Ahead* (right column). The bottom two panels summarize AIA 193 Å observations—we shall return to those below.

For each of the panels (a)–(l) in Figure 16 we took a series of *STEREO A* or *B* images and determined the intensity signal (in arbitrary units) on a ring centered on the Sun at distances, from top to bottom, of 8, 5, 2.2, 1.8, 1.15, and 1.05 solar radii

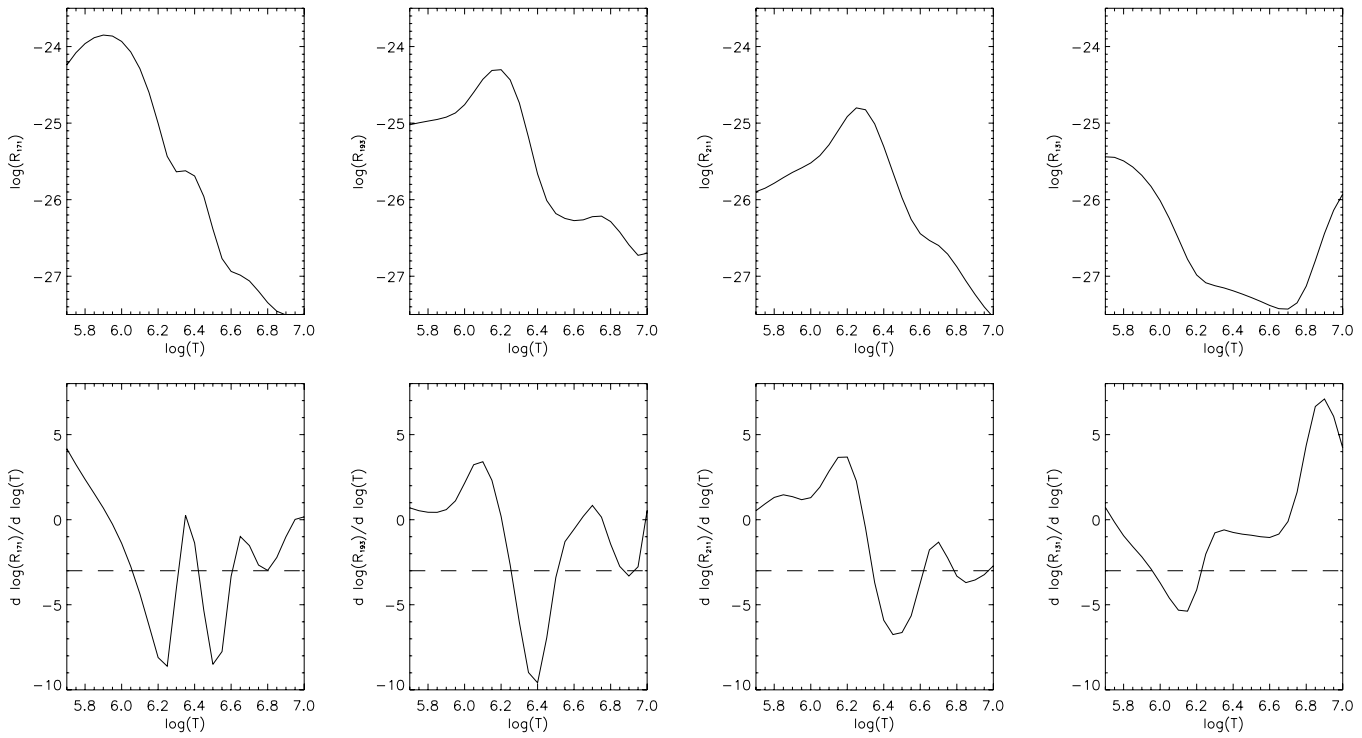

Figure 13. Thermal responses for (from left to right) the AIA 171, 193, and 211, and 131 Å channels. The top panels show the logarithmic filter responses, $^{10}\log(R)$, in DN cm^5 s^{-1} pixel^{-1} (using the SSWIDL procedure aia_get_response.pro). The bottom row shows the corresponding derivatives $d\ln(R)/d\ln(T)$ (see Equation (2)); horizontal dashed lines indicate a value of −3 (cf. Section 5.1).

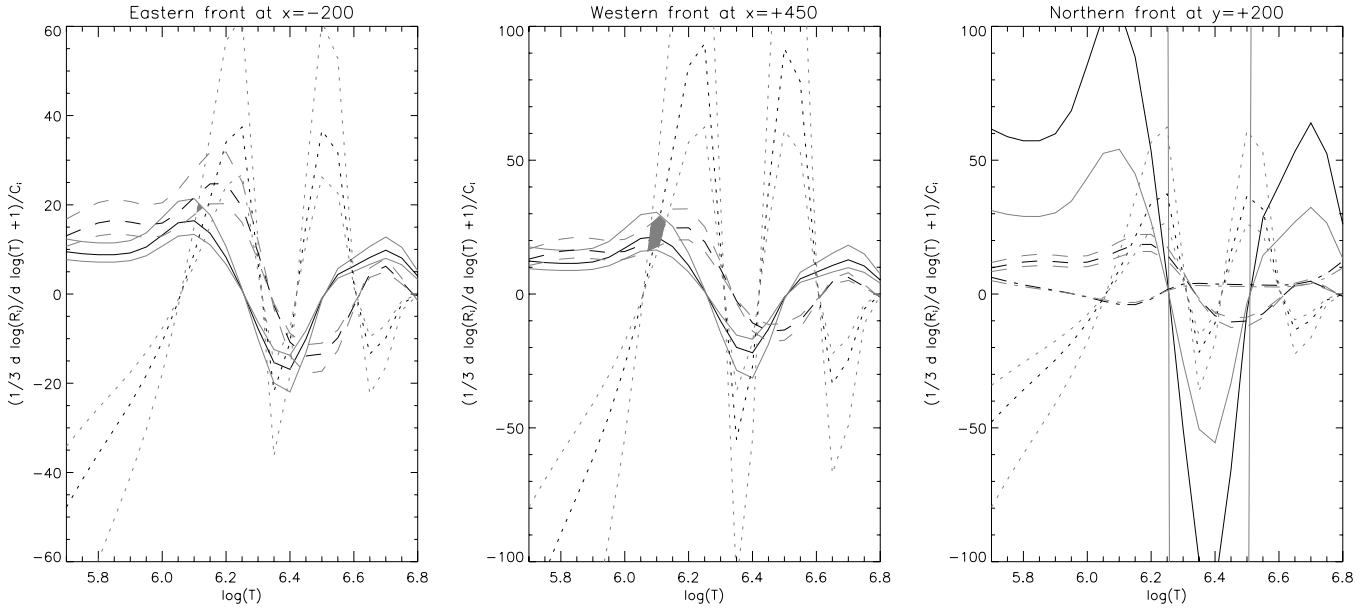

Figure 14. Expressions of Equation (4) (black curves) for the trailing edges of the three fronts marked in Figure 12 for the estimated intensity contrasts (with uncertainties in gray) listed in Table 2 (which also identifies the line types used). Intervals with solutions consistent with the isothermal adiabatic assumption are shaded in the left two panels. In the right panel, the 131 Å solutions lie outside the constraints shown by the gray curves, i.e., there is no solution consistent with the isothermal adiabatic approximation.

from the disk center using COR2 for the first two, COR1 for the next two, and 195 Å for the third pair. These concentric rings are shown to scale in Figure 4(a). We then made first-difference images and show these as gray-scale images with positive changes (brightenings) as lighter shading.

The horizontal axes in all panels are in latitudinal degrees. In the left-hand column, zero is at the solar equator facing Earth; to avoid confusion, that direction is at 180 for the *STEREO A* images on the right. We inverted the handedness of the rotation angle for the *STEREO A* images so that the images have a readily comparable orientation relative to those from *STEREO B*. The vertical axes in the panels are in decimal UT hours counting from 2011 February 15 00 UT; the bottom of each of the panels is at 01:44 UT, the start time of the *GOES* X2.2 flare according to the NOAA reports. Note that the vertical range increases in the panels from bottom to top.

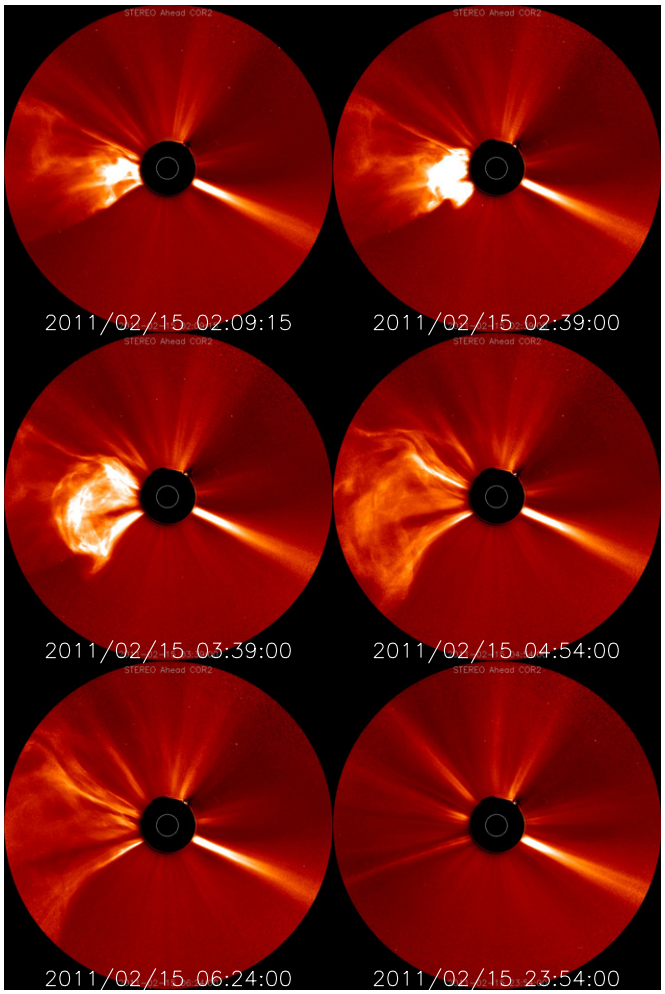

Figure 15. Composite of images taken by *STEREO A*/COR2 (times are shown on the images). Movies 8 and 9 show the *STEREO A*/COR2 and *STEREO B*/COR2 movies, respectively, for 2011 February 15.

(A color version and animations (Movie 8, Movie 9) of this figure are available in the online journal.)

In the COR2 image sequences in particular, the CME shows as an outward traveling bulge, behind which two well-defined intensity structures remain at nearly fixed position angles for many hours after the bulge passes by. The position angles of these structures—the post-CME flanks—at 8 $R_\odot$ are shown by the vertical white–black dashed lines, repeated in each of the panels below the top one. Note that there is a slight offset of the difference signal as one approaches the Sun; we think this reflects a slight bend in the field structure toward the ecliptic from the solar surface outward (but the effect is small, at most 5° from 1.8 to 8 $R_\odot$).

The bottom two panels of Figure 16 are running-difference images rather than first-difference images (there is too much change to make the first-difference images useful for the analysis of the perturbation front) for the AIA 193 Å channel. For this purpose, we used the signal on the central meridian (Figure 16(m), enlarged in Figure 17) and at 25° west (Figure 16(n)) for the set of fixed-exposure time images; following an intermediate meridian across the flaring region caused too much CCD-bleed interference, while using the variable exposure time images caused problems with the signal's zero point). Note that the horizontal dashed line shows the peak time for the *GOES* flare.

The bottom panels (and the enlarged version in Figure 17) show clearly defined slanted ridges (below which a reference white–black dashed line is shown to guide the eye, offset downward for display purposes by 6 minutes). In Figures 16(m) and (n), we see the northward-propagating perturbation front (note that it starts after the flare start but well before the flare peak in *GOES* X-rays). The southward-propagating front is hard to see across the central meridian (Figure 16(m)), but is there as a more diffuse pattern at lower signal. This front is readily recognized at 25° west, however, as shown in panel *n*. The track of the ripple (the slanted dashed line) is repeated in each of the panels. For EUVI/193, there is no significant delay in when the signal appears (given the relatively low EUVI cadence), but above that, time delays are readily measured. The slant of the ripple has the front propagate at a speed of 215 deg hr^{-1} or 730 km s^{-1} projected onto the surface. Judging by the radial advance of where the expansion is first seen, we estimate an average velocity of about 1150 km s^{-1} (but see Figure 9 discussed below).

The "standard" exposure time used in the AIA channels (alternating with exposures with variable duration under automatic exposure control) was 2 s. For speeds up to 730 km s^{-1}, this would cause motion blurring of approximately 1460 km, equivalent to 3.3 pixels. At a cadence of 24 s, this would advance the front on successive images by approximately 40 pixels. Note that we do not see signatures so narrow in either the direct imaging or in the running-difference sequences.

We point out one other feature in Figure 16. In COR1 (most easily in *STEREO B*), also vaguely in COR2 at 5 $R_\odot$ and possibly with a hint in EUVI/193 at 1.15 $R_\odot$: a faint northward extension that extends to almost 100°, i.e., reaches at least the north polar regions. The propagation speed of this feature is much lower than that of the front seen in the AIA images and the *STEREO* EUVI images around disk center as seen from Earth (compare the slope of the feature with the dashed slanted line segment which shows the propagation speed of the latter): for the *STEREO-B* COR1 data at 1.8 and 2.2 $R_\odot$, we estimate the average speed from flare onset to be about 80 ± 10 deg hr^{-1} (490 ± 60 km s^{-1} if propagating at 1.8 $R_\odot$). This compares well with the very faint, far-propagating features toward the east and west seen in the *STEREO-A/B* 195 Å images discussed in Section 5.1. We return to this in Section 7.1.4.

5.3. History of Expansion from Rope to CME

The expansion history of the flux rope, of the propagating EUV front, and of the front of the outward-moving CME is compared to each other in Figure 9. This figure shows the results of expansion of the flux system in the core of the active region discussed in Section 4 and shown in Figure 8, as well as the position of the propagating EUV front as discussed in Section 5.2 and shown in Figure 16(m).

Figure 9 also shows the evolution of the CME. The times at which the expanding front was first seen in the *STEREO* COR1, 2, and EUVI/193 time slices as a function of the radial distance (at 1.05, 1.15, 1.8, 2.2, 5, and 8 solar radii) are plotted against the distances from the center of the flare-ribbons site in Figure 9.

Note how well the positions of the southward expanding loops tracked in the AIA 335 Å images continue in the northward-propagating bright coronal front (both measured from the Earth perspective as features projected against the disk) and how well that lines up with the radial expansion measured in the *STEREO A*/COR1 and COR2 observations.

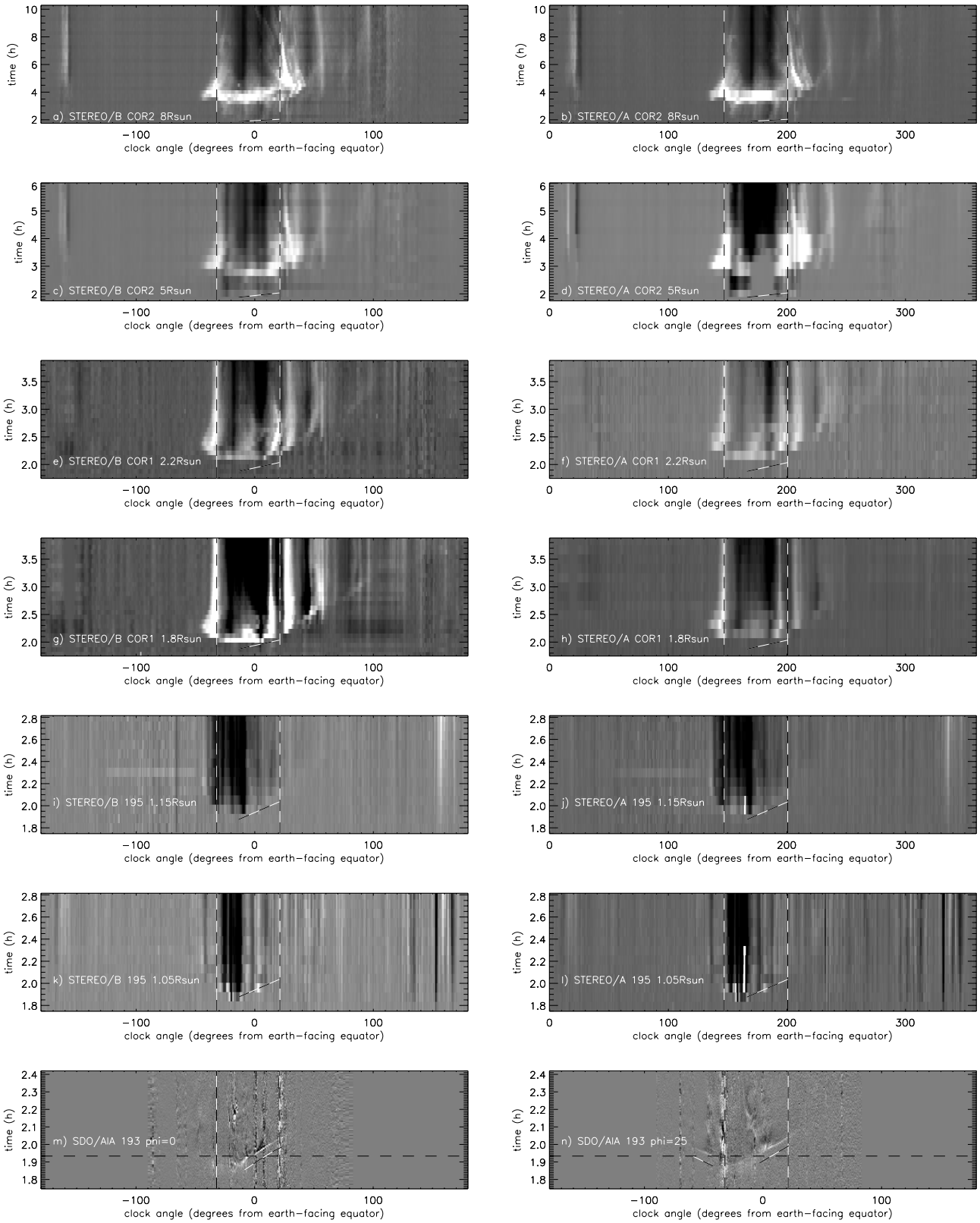

Figure 16. (a–l) First-difference time slices for data taken by *STEREO B* (left column) and *STEREO A* (right column). Each of the panels shows the intensity signal in COR2, COR1, or EUVI's 195 channel on concentric circles around the Sun (see illustration in Figure 4(a)). The horizontal axes show position angle around the Sun, relative to the Earth-facing solar equator for *STEREO B* and 180° away from that for *STEREO A*. Increased and decreased brightness is shown bright and dark, respectively. Vertical dashed lines show the position angles of the bright "stalks" seen late in the event at 8 solar radii in COR2/B images (in Figure 15). (m, n) Running-difference images for AIA 193 Å images across central meridian (m) or 25° west longitude (n); image pairs were used with a temporal spacing of 96 s. The dashed curve in (m) is an approximation to the ridge in the running-difference image, displaced downward by 0.5 h for clarity; a linear approximation to that curve is repeated in all other panels to provide a reference. See Section 5 for further details. Movie 4 shows composites in Fe XII channels of the full-disk images from AIA (193 Å channel, center) and the *STEREO* EUVI (195 Å channels) for *STEREO B* (left) and *STEREO A* (right). The hemispheres visible from the *STEREO* perspectives are indicated by the white segments of the circles, which represent the Sun seen from above with Earth viewing it from below.

(An animation (Movie 4) of this figure is available in the online journal.)

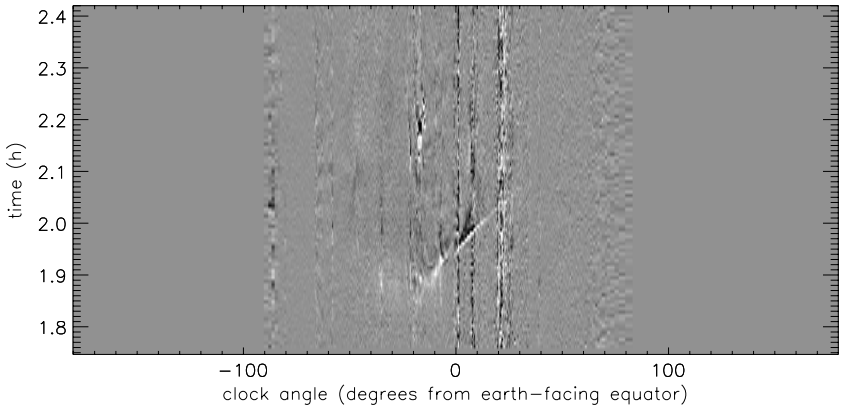

Figure 17. Magnified repeat of Figure 16(m).

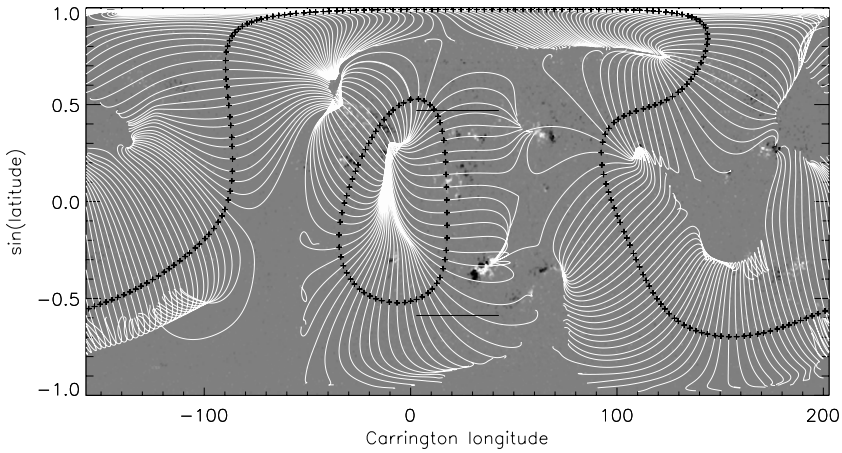

Figure 18. Full-sphere magnetic map and select PFSS field lines, rotated so that disk center is in the center of the frame. The field lines shown are those that extend downward from the source surface (set to 2.5 $R_\odot$ from Sun center) starting from a set of locations at which the radial field vanishes (i.e., the base of the heliospheric current sheet beyond the PFSS modeling volume); loop tops are indicated by plus symbols. Horizontal black line segments show the latitudes of the streamer stalks marked by dashed lines in Figure 16.

Figure 9 combines our measurement for three fundamentally different aspects of the eruption: loops that are part of what appears to be a flux rope as the source of the eruption, an expanding intensity front propagating away from the flaring active region seen on disk, and the leading edge of the intensity signature of the CME propagating outward from the Sun into the heliosphere. The relatively continuous connection between expanding loops, propagating coronal front, and CME signifies that we are indeed looking at closely related features at the outer envelope of the event. We note that the three distinct features need not be identical: uncertainties in timings and the imperfect continuity of the data in Figure 9 are substantial enough that, for example, the expanding loops and the coronal propagating front may have some distance between them, as the modeling discussed in Section 7 suggests.

The dotted line in Figure 9 is a power-law approximation to the distances from the flare sites, measured from a reference time of 01:47:30 UT (when the flare-ribbon kernels become bright enough to exhibit clear diffraction patterns in the AIA images; see Section 5.1):

$$d[\mathrm{km}] = 1.16\,10^4 (x[\mathrm{min}])^{1.38}. \quad (5)$$

The associated derivative, i.e., the velocity profile, is shown in the bottom panel of Figure 9 for reference.

6. CORONA TO HELIOSPHERE: POTENTIAL-FIELD SOURCE-SURFACE MODEL

Figure 18 shows a full-sphere synoptic map (Schrijver & DeRosa 2003, Schrijver & Title 2011) based on *SDO*/HMI LOS magnetic field observations. The map has been shifted so that the central meridian at the time of the 2011 February 15 X2 flare is in the center. Superimposed on this image is a set of field lines based on a potential-field source-surface approximation with the source surface set at 2.5 solar radii from the Sun's center (Schrijver et al. 2002). The field lines shown are those that touch the source surface at their tops, and are thus the PFSS equivalent of the streamer belt at the foundation of the heliospheric current sheet across which the radial component of the heliospheric magnetic field changes polarity.

The tops of these field lines, shown by plus symbols, outline the positions on the source surface where the radial field vanishes. Below this set of field lines all field is closed, while outside of it part of the field connects to the heliosphere.

The configuration of the PFSS helmet structure is unusual for this model for 2011 February 15: apart from the normal slowly undulating large-scale structure, there is an island structure with a ring-shaped arcade somewhat to the north and east of disk center (Schrijver 2005 quantifies how rare such topological features are). The eruption from AR 11158 occurs underneath

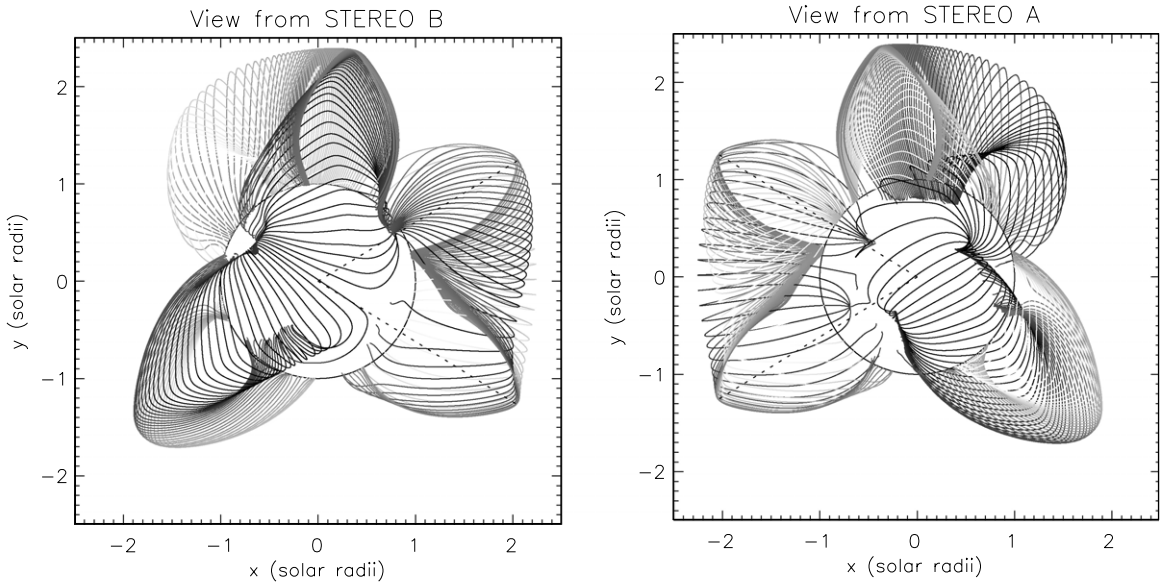

Figure 19. Rendering of the field lines shown in Figure 18 from the perspectives of *STEREO B* (left) and *STEREO A* (right). The field lines are coded such that the nearest segments are black and the furthest segments white. Dotted line segments connect disk center with the tops of the Earth-facing ring-shaped helmet structure seen in projection against the sky.

this structure, and thus must disrupt the closed field in order to escape into the heliosphere.

Several hours after the CME, the bright structures seen in the *STEREO A*/*B* COR2 images at 8 $R_\odot$ (marked by the dashed lines in Figures 16(a–d)) occur at latitudes 32°S and 21°N. Around 2.2 $R_\odot$, the COR1 images show these flanks to be somewhat wider, with mean latitudes of 38°S and 27°N. These latitudes correspond roughly to the southern and northern extremes, respectively, of the oval of the PFSS helmet streamer structure (compare the horizontal line segments in Figure 18 with the source-surface null line indicated by the plus symbols.

The two panels in Figure 19 show the PFSS helmet-streamer fields projected as viewed from the perspectives of *STEREO B* (left) and *A* (right), respectively. The dashed lines connect the disk center to the apparent tops of the Earth-facing helmet-streamer structure seen in projection against the sky. These directions are within half a degree from 32° N and S latitudes.

The differences between the extreme ranges of the ring-shaped helmet-streamer structure seen in the synoptic map of Figure 18, in projection against the sky in Figure 19, and the sensitivity of the overall structure to details in the surface field (including the polar-cap strengths and the process by which the apparent monopole is corrected for), suggests that the CME propagates outward to a latitude range that is set by the foundation of the coronal field a few solar radii above the solar surface.

7. INTERPRETATION GUIDED BY MHD MODELING

7.1. Flux-rope Eruption from the Perspective of AR-scale Modeling

7.1.1. Model Description

We use the three-dimensional zero-β MHD simulation of solar eruptions that is extensively described by Aulanier et al. (2010) to guide the interpretation of the observed features. In this MHD model (visualized here in Figure 20), a pre-eruptive, weakly twisted coronal flux tube gradually forms and grows both in height and length along the photospheric inversion line, within an asymmetric bipolar region. The photospheric field is driven by slow line-tied motions and magnetic field diffusion in the photosphere (in a similar way as modeled by van Ballegooijen & Martens 1989, Amari et al. 2003, and Mackay & van Ballegooijen 2006), as observed by HMI for several days prior to the 2011 February 15 flare (see Section 4). The flux rope eventually erupts when its axis rises above a critical height, which corresponds to the threshold for the torus instability (Kliem & Török 2006), that has further been shown to be equivalent to a catastrophe or loss of equilibrium (Démoulin & Aulanier 2010). As in all realistic CME models, the modeled eruption leads to the rise of the initial rope, to the pinching and reconnection of the underlying field lines that result in forming post-flare loops and in feeding the flux rope, and to the expansion of the surrounding arcades that are carried upward and sideways along with the inner rope.

In this particular model, owing to the combined effects of the slow growth rate of the eruption and of the prescribed coronal density profile, the eruption is gradual, and always remains sub-Alfvénic inside the computational domain (which is 15 times as high as the initial horizontal distance between the centers of the two photospheric flux concentrations). So there is neither a high-wavenumber freely propagating wave launched by the flare reconnection or by the CME expansion, nor a CME foreshock at high altitude. The outer faces of the model domain are open, so that the magnetic configuration includes some "open" field lines right from the beginning of the simulation. This boundary condition allows the expanding structures to leave the domain freely without generating significant compressive and inductive artifacts near the boundaries.

It is worth noting that the model does not treat the quadrupolar nature of the active region. This quadrupolar topology is probably responsible for the development of the arc-shaped secondary ribbons. Indeed, following some MHD simulations of quadrupolar reconnection (Aulanier et al. 2005) and some *TRACE* observations of another similar event, supplemented by potential field extrapolations (Chandra et al. 2009), we argue that the appearance of the secondary ribbons is caused by the reconnection of some expanding field lines, rooted in

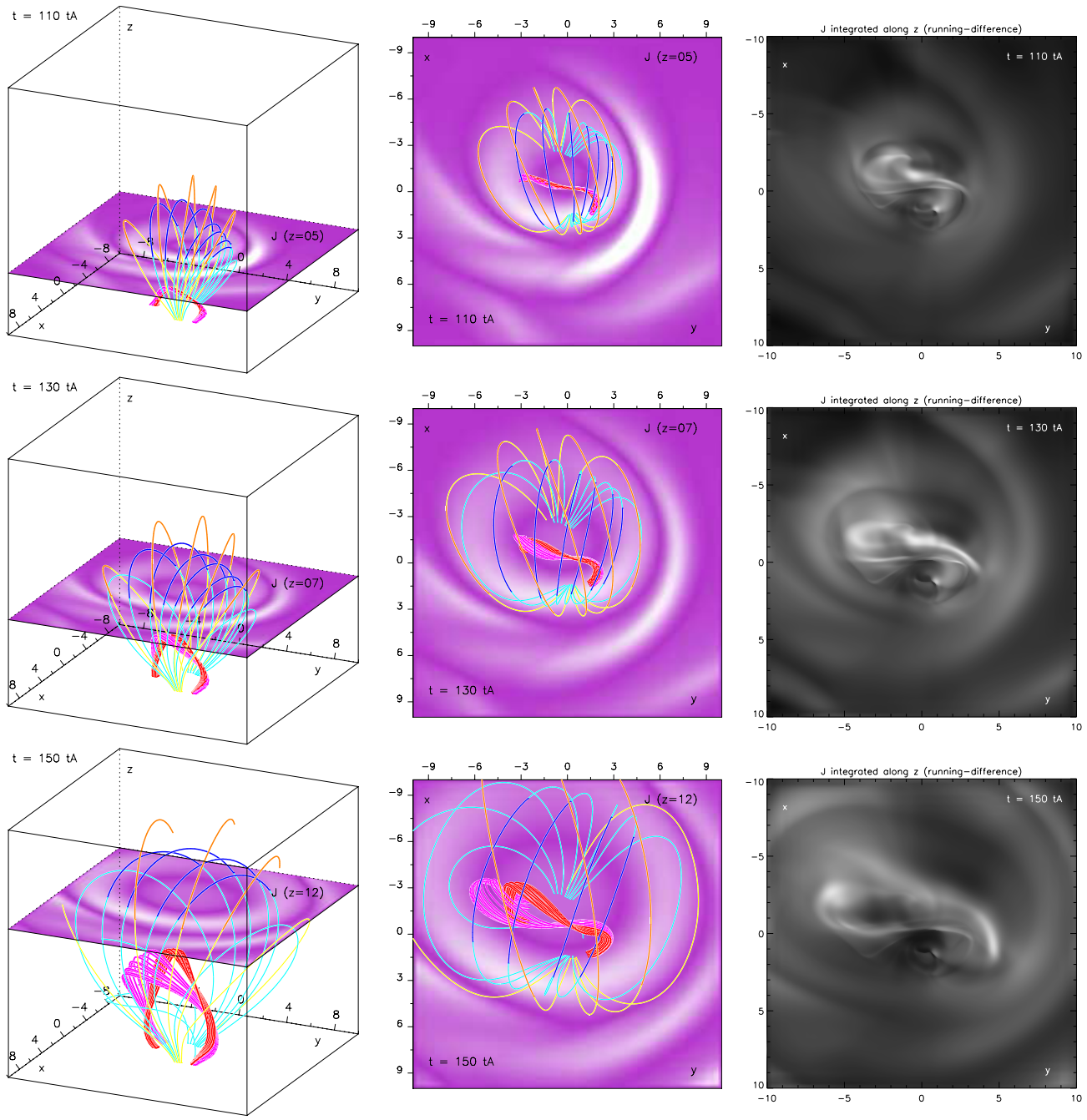

Figure 20. Expansion of the current shell and associated field lines during the eruption in the MHD model, at three times $t = 110, 130, 150\,t_A$. The left and middle columns show projection and top views of representative field lines, and a purple rendering of horizontal cuts of the electric currents J. The pink and red field lines trace the inner flux rope, which is anchored in the hooks of the QSL (plotted in Figure 21). For reference, these lines are the same as plotted in Figure 2 from Aulanier et al. (2010). The cyan-blue (resp. yellow-orange) field lines are large-scale weakly sheared (resp. nearly potential) arcades located just inside (resp. around) the shell. At each time t, these field lines change color when they cross altitude z of the horizontal cuts for J, which corresponds to a section of the shell in its upper half. The right column shows a series of running-difference images of the vertically integrated currents J at three times, with a linear gray-scale rendering the change in currents at reduced contrast, showing $[\int J(t)dz]^{1/4} - [\int J(t-5t_A)dz]^{1/4}$.

(A color version of this figure is available in the online journal.)

the inner δ-spot, with outer field lines rooted in the outer bipole. There is, however, no reason for this effect to alter the interpretations given hereafter for the observed features summarized above. Note also that, unlike in the MHD model, this complex environment could a priori be the cause of the eruption itself (according to the breakout model of Antiochos et al. 1999), but this seems not to be the case in this event. Indeed, Movie 3 suggests that the secondary ribbons start to brighten about 2 minutes after the double-J flare ribbons which, following Li et al. (2006) and Ugarte-Urra et al. (2007), implies that this eruption was not caused by the magnetic breakout.

7.1.2. Quasi-separatrix Layers Footprints as Flare Ribbons

As mentioned in Aulanier et al. (2010), from the time $t = 76\,t_A$ onward (with time expressed in characteristic Alfvén times, which is defined as the transit time of Alfvén waves over half the distance between the polarity centroids), not only before the modeled eruption occurs but also after it is triggered

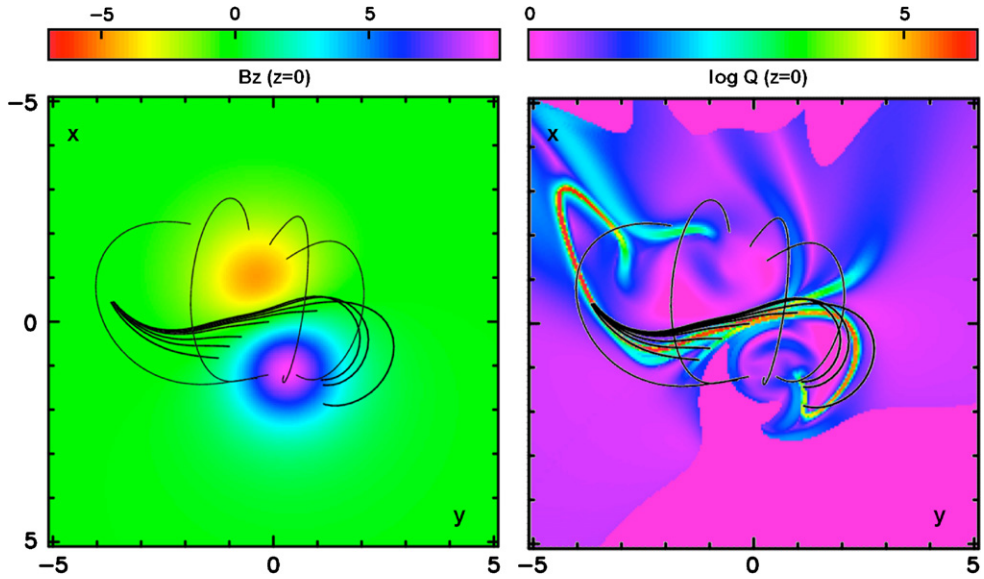

Figure 21. Top view of the pre-eruptive magnetic field configuration at $t = 90\,t_A$ in the MHD model. The thick lines (running mostly east–west) are located in the quasi-separatrix layer (QSL) and the thin lines (predominantly north–south) are weakly sheared overlying arcades. The left panel shows the synthetic magnetogram for the LOS field component and the right panel shows the QSL footprints expressed through the squashing factor Q (Titov 2007).

(A color version of this figure is available in the online journal.)

at $t = 110$–$120\,t_A$, the weakly twisted core flux rope is separated from its surrounding nearly potential (but still weakly sheared) coronal loops by a quasi-separatrix layer (QSL). QSLs are narrow volumes within which the field-line connectivity varies strongly but continuously. The QSL incorporates a hyperbolic flux tube (HFT). The latter shows up as an X-point as viewed in projection along the rope axis, but because the field is fully 3D, there is no true null point but rather a strong so-called guide field along the HFT. The QSL footprints are shown in Figure 21 at $t = 90\,t_A$ just prior to the eruption. They correspond to the narrow regions where the QSL squashing degree Q (as defined by Titov 2007) at the base ($z = 0$) is the highest (Q in Figure 21 is calculated with the same mesh-refinement iterative method as described by Aulanier et al. 2005).

The QSL footprints display an asymmetric double-J shaped pattern, which is the same as that found earlier for symmetric flux rope models by Démoulin et al. (1996) and Titov (2007): the hooked section of each J whirls around the flux rope, and the nearly straight parts of the J's surround short arcades rooted on each side of the photospheric inversion line and thus being located below the coronal HFT. Following Aulanier et al. (2005), we highlight in Figure 21 the connectivity variations across the QSL by plotting a fan of field lines with footpoints along a short segment that crosses the QSL around $x = -0.5$ and $y = -3.8$, in regions where $Q > 10^4$ and where the vertical component of the photospheric magnetic field is $B_z(z = 0) < 0$. These field lines diverge and map to stronger $B_z(z = 0) > 0$ areas, all along the conjugate J-shaped QSL footprint, both along its straight part and its hook. The same diverging-remapping pattern can be obtained for any fan of field lines that cross the QSL footprint at any position.

Reconnection can happen in QSLs, as argued by, e.g., Aulanier et al. (2006, 2007). This indeed happens in the simulation discussed here, as post-flare-like field lines are gradually formed below the rope a little before and mostly during the eruption, through magnetic reconnection between J-shaped sheared field lines (as previously illustrated in Moore et al. 2001). It has also been shown, thus far for confined flares only, that QSL footpoints can correspond to observed flare ribbons (among numerous studies, see, e.g., Schmieder et al. 1997 and Masson et al. 2009). By extension, it is arguable that the double-J-shaped QSL footprints first put forward by Démoulin et al. (1996) can correspond to double-J-shaped flare ribbons associated with eruptions, as argued by Chandra et al. (2009) and as clearly shown here in Movie 3.

One key and unprecedented observational feature here that supports this scenario is the existence of hot coronal loops, mostly visible with AIA at 335 and 131 Å (see Movie 3), which all seem to emanate from the same small region around the easternmost part of the bright hook of the northern J-shaped ribbon, and which apparently map down all along the southern J-shaped ribbon. Even though it is difficult to see this diverging-remapping loop pattern on single AIA frame, Movie 3 strongly suggests that it exists. This observed pattern is very suggestive of the modeled one as plotted in Figure 21. It could probably not be observed by past solar EUV imagers such as *TRACE*, or with the lower spatial resolution of EIT and EUVI, because none of these has the sensitivity and high-temperature response of AIA.

This newly observed diverging-remapping loop pattern therefore directly supports that the J-shaped ribbons are cospatial with the footprints of a QSL that surrounds the initial flux rope that rises and erupts, and that the X2.2 flare is produced by QSL reconnection. This now allows us to infer that the different sets of coronal loops that are seen to expand above the flare site in the early stages of the eruption, as observed in hot (335, 94, 131 Å) and in warm (211, 193, 171 Å) AIA channels as being rooted away from the J-shaped ribbons, must correspond to large-scale field lines that are located far above the initial flux rope, both before and during the eruption. This is an essential step in our interpretation of the coronal propagation front, as it will show that the front originates neither from the flare site itself nor from the sides of the core flux rope.

7.1.3. An Expanding Shell of Return Currents as the Propagation Front

As argued in Section 7.1.2, different sets of large-scale coronal loops, anchored in the photosphere far from, and passing in the corona significantly above, the erupting twisted flux rope,

are seen to expand in all directions above the active region during the eruption. Both *SDO*/AIA (Movie 3) and *STEREO A*/EUVI (Movie 4) show that these expansions start around 01:47 UT, coinciding with the beginning of the brightenings of the flare ribbon, several minutes before the flare peak (see Table 1 and Figure 7), as discussed in Section 4. Two of the most striking things observed by AIA, which maybe are most clearly seen in the 2MK 211 Å channel (Movie 2)—possibly owing to its good contrast and relatively weaker CCD saturation from the flare—are that:

1. between 01:50 and 01:53 UT, the active region-scale expanding loops start to lose their identity, while they form all together an envelope which looks like an expanding bubble, as viewed from above. This expanding bubble is also clearly seen from the side with EUVI, at its much lower cadence (see Movie 4); and
2. between 01:53 and 01:54 UT, these same loops vanish nearly completely while the arced front which encircles them, and therefore the bubble in which they have turned into earlier, eventually turns into the coronal propagating front.

When combined with EUVI observations (Figure 15 and Movie 4) these observations strongly suggest that the propagation front is formed just at the edges of the large-scale expanding active region loops that surround the inner flux rope.

This is reminiscent of the current-shell model for propagating parts of "EIT waves" (Delannée et al. 2008). This model states that coronal propagation fronts are formed by Joule heating and/or plasma compression, which both occur within a high-altitude expanding and narrow shell, which is located in the thinning layer of return (or neutralization) currents that surround the erupting flux rope, separating it from the surrounding, untwisted fields. Even though Delannée et al. (2008) argued that this shell should be a generic property of all eruption models, we know of no other MHD simulations at present which have addressed this. We therefore searched for the existence and properties of such a shell in the simulation of Aulanier et al. (2010), which is a more realistic eruption model than the one calculated by Delannée et al. (2008), although it does not follow the eruption up to altitudes as high as considered by those authors. Figure 20 shows the result of this search.

The model exhibits an expanding current layer at high altitude, located between the large-scale weakly sheared relatively low-lying field lines (shown in cyan/blue) and the overlying nearly potential arcades (shown in yellow/orange). This is significantly above the inner flux rope (which is shown in pink/red) that lies rooted in the hooks of the QSL. In this current shell, the field-aligned components of the electric currents are flowing anti-parallel to the magnetic field. Because the magnetic helicity of the system is positive (the flux rope is right-handed and the double-*J* QSL/ribbon pattern forms a forward-S, both typical of the southern solar hemisphere), the currents in the shell are return currents. We note several slight differences with the MHD simulation of Delannée et al. (2008):

1. Owing to the lack of symmetry in the magnetic field and the absence of twisting in the strongest magnetic fields, the return currents here form a complex pattern at the photosphere (see the top panels in Figure 6 of Aulanier et al. 2010) that does not simply surround the strong fields of the photospheric bipole.
2. Because of the different photospheric driving and eruption mechanisms, the inner flux rope in the model discussed here is much smaller, and therefore well separated from the overlying current shell. As viewed in Figure 20 with high-altitude cuts along (x, y) horizontal planes, or as vertically integrated currents, the current shell forms a full oval structure that surrounds the inner rope.
3. Because of the relatively small numerical domain in the horizontal (x, y) directions, the simulation discussed here cannot follow the expansion of the CME up to very large horizontal distances. Figure 20 indeed shows that the shell reaches the edges of the domain around $t = 150\,t_A$. This limits the analysis of the buildup of the shell to its early stages. This may explain why the overdensities that are expected to form inside the shell, as calculated by Delannée et al. (2008), are not obviously noticeable in this model. Nevertheless, the horizontal velocities outside the shell decrease between $t = 130$ and $150\,t_A$, which suggests that if the expansion could be followed for longer times, plasma compression might develop there, as it did in the model by Delannée et al. (2008).
4. There is another outer current shell, although it does not completely surround the eruption, because it only displays an arc-shaped current pattern in the $y > 0$ part of domain in Figure 20. This arc-shaped layer forms at the interface between initially closed field lines which have both footpoints rooted at $z = 0$ and initially open field lines which leave the domain through one of the outer open boundaries.

The substantial spatial separation between the core flux rope and the overlying arcade that forms the current shell is the key to linking the theoretical (MHD) and the observational (AIA and EUVI) interpretation of the coronal propagating front. Both approaches lead to the same conclusion: the propagation front is the manifestation of an optically thin shell, seen as a bright oval in projection above the solar disk and as a bubble from the side above the limb, that forms in a narrow layer of enhanced electric currents, and maybe at later times of plasma compression, that are located within the expanding interface between large-scale weakly sheared loops and their surrounding current-free arcades. Both the model and the observations for the front moving across quiet-Sun regions are compatible with a plasma warming process within the front; this warming makes it brighter (resp. dimmer) at 211 and 193 (resp. 171) Å, which was hinted at by early *SoHO* observations (Wills-Davey & Thompson 1999) but clearly seen by AIA, and likely hotter in the region between active regions as seen by a weak brightening in 131 Å. Being zero-β, and not being able to follow the formation of clear plasma compression within the shell, the model cannot resolve whether the warming of the shell is of adiabatic nature (as explicitly calculated in Downs et al. 2011—see Section 7.2), or is caused by Joule heating, or both. The observations of the 2011 February 15 events suggest that adiabatic warming is consistent at least with the observations of the coronal propagating front over quiet Sun (east–west directions); some heating in addition to adiabatic warming by compression may well be required for the northward-propagating segment of the front (the magnitude of such heating would need to be established jointly with an evaluation of the validity of the isothermal assumption for that environment; see Section 5.1).

7.1.4. MHD Perspectives on Intermediate Scales

At later times, on the global scale, the coronal propagating front is seen to halt at the edges of the surrounding streamer, as revealed from *SDO* and *STEREO* observations and the

PFSS extrapolation (Section 6). This large-scale configuration is not treated in the MHD model of Aulanier et al. (2010). Nevertheless, the present observations and model are consistent with the scenario previously put forward by Delannée & Aulanier (1999) and Delannée et al. (2007), and probably taking place in the large-scale MHD simulations of Downs et al. (2011), discussed next in Section 7.2: regardless of resistive phenomena, the expanding and accelerating current shell can eventually encounter most of the streamer-type field lines at the scale of the solar radius, over a wide range of longitudes and latitudes owing to the shell expansion, and then can push these streamer field lines from below, eventually turning them into the outer envelope of the CME. In this context, the flanks of the CME front as well as the final horizontal extent of the coronal propagation front should naturally correspond to the lower part of field lines forming the streamer boundary, because those are the last closed field lines that the bubble/shell expanding from the active region encounters before reaching the solar wind open field lines.

Finally, we comment on the very faint, far-propagating perturbations that are seen to reach the north polar regions and the eastern and western limbs for the Earth's perspective, as we described in Sections 5.1 and 5.2 (see Figures 10 and 15 and Movies 4, 8 and 9). The data in Figure 16 show the northward-propagating signature of this feature most prominently at 1.8 $R_\odot$ and beyond, with at best a faint suggestion at lower heights. While one might argue in favor of a magneto-acoustic wave hypothesis to explain these features, the PFSS model (Figure 5) can also be interpreted as a lateral compression of plasma surrounding the erupting streamer (i.e., the CME) against the enveloping streamer belt toward the east, north, and west. The latter interpretation is consistent with the absence of a perturbation close to the south pole, because there is no streamer there close to the southern boundary of the CME. We leave these faint, far-propagating perturbations for future study, as the focus of the present study is the study of the erupting volume and its transition into a CME.

7.2. The Perspective of Global MHD Modeling

Downs et al. (2011) use a 3D MHD code to experiment with parameters within a simulation of a CME and "EIT wave," specifically for events toward the end of 2008 March 25, starting from a full-sphere synoptic map for Carrington rotation 2068 based on *SoHO*/MDI measurements. They simulate the eruption, and visualize it as it would be observed in *STEREO A*/*B*–EUVI observations in the 171, 195, and 284 Å (Fe XV) channels. They then compare simulation results while varying the eruption strength (defined by the flux in the erupting source region), the handedness of the field configuration (which affects the interaction between the ambient and erupting fields), and the fast-magnetosonic wave propagation speed (by changing the ambient coronal field strength).

Their modeling shows that a density enhancement ("compression front") envelops the erupting volume. For the characteristic quiet-coronal plasma temperature chosen for the ambient, pre-eruption corona, the compression front manifests itself as a dimming in 171 Å and a brightening in the higher-temperature 195 and 284 Å channels, similar to what we observe for the 2011 February 15 front (replacing AIA's 211 Å, dominated by Fe XIV, for EUVI's 284 Å, dominated by Fe XV). The thickness of the compression front (estimated from the temporal profile in their Figure 8 and the rise speed given in their Table 1) is approximately 200–300 arcsec (depending on the model parameters), which compares favorably with the thickness of the intensity enhancements seen in Figure 12 for the 2011 February 15 coronal propagating front.

Experimentation with the magnetosonic speed shows that a fast-magnetosonic wave front and a compression front can be shown to propagate at the leading edge of the eruption, provided that the magnetosonic speed is sufficiently higher than the speed of the erupting volume. The observational signature of the leading magnetosonic wave in the simulated EUV images is, however, found to be insignificant relative to the signature associated with the compression front. In this context, we note that the parameter domain explored in their simulations means that the "transverse speed of the compression front in the quiet-Sun is below the typical fast magnetosonic speed;" for higher eruption speeds, the compression front would be surrounded by a shock wave with no possibility of a leading magnetosonic wave.

The modeling by Downs et al. (2011) also exhibits a modulation of the streamer structure, much like we noted above for the 2011 February 15 CME: the propagating CME causes the streamer to temporarily bulge outward as it responds to the expanding compression front, and then relax back to its initial position angle. From this behavior, they conclude "that the observed EUV wave signature is most closely related to the plasma compression of the streamer region (surrounding field) as it is perturbed from an equilibrium state."

8. CONCLUSIONS

8.1. The Events on 2011 February 15

We present observations of a large X-class flare, CME, and "EIT wave" observed on 2011 February 15. The expansion of the core field of AR 11158, straddling a highly sheared strong-gradient polarity inversion line between the central spot clusters of a double bipolar region, begins at the time when the first flare ribbons become visible. The X-ray brightness of the X2.2 flare as measured by *GOES* and, for example, the 335 Å solar irradiance as seen by AIA increase for the following 10 minutes, at which time the flare ribbons reach their maximum extent.

The expansion of a volume of loop structures from the core of the active region (AR) shows a rapid (power-law) increase of the velocity up to at least 500 km s^{-1} before the individual features are no longer identifiable. This expansion continues smoothly into a coronal propagating perturbation that appears to travel most obviously some 50 to 100 Mm above the solar surface. This coronal propagating front (known as "EIT wave") is visible out to almost a full solar radius from the flare site, apparently continuing to increase in velocity, albeit not isotropically. The 171, 193, and 211 Å signals suggest that this front is associated with an increase in temperature, and thus mostly a dark front in 171 Å (dominated by Fe IX and Fe X) and a bright front in 193 and 211 Å (dominated by Fe XII and Fe XIV), but hot enough to show up in 335 Å (dominated by Fe XVI) and weakly in 131 Å (Fe VIII and Fe XXI) along the northern and southern parts of the front but not in the eastern and western directions. A thermal analysis suggests this temperature rise is consistent with predominantly adiabatic compression of the inner edge of the expanding volume (subject to uncertainties in response functions and the approximating assumption of isothermal plasma) at least for the front propagating through the quiet-Sun corona.

The front continues to propagate away from the flare site until it extends over an opening angle as seen from Sun center that corresponds to the range over which a circular helmet structure

of closed field exists according to a PFSS model (in line with the conclusions of, e.g., Delannée & Aulanier 1999 and Delannée et al. 2007). This ultimate opening angle matches the flanks of the inner-heliospheric structures seen before and after the eruption at the northern and southern extremities of the PFSS helmet arcade that needs to be opened for the eruption to be able to reach into the heliosphere. A bulge is temporarily seen beyond this opening angle as the eruption moves through, but the field topology appears to be able to contain the eruption to the bounds of the helmet structure.

The erupting structure behaves as a not-quite isotropically expanding, rising volume of which the lateral expansion is eventually limited to the geometry of the containing helmet structures, although there is a temporary overshoot beyond that, but not likely beyond the bounds of the outer footprint of the helmet-structure oval.

The expansion of a volume filled with active-region loop, the ensuing coronal perturbation front, and the expansion of the eruption into a coronal mass ejection transition into each other remarkably smoothly, but—according to the model interpretation—not quite continuously. The close, but not perfect, correspondence of expansions seen in the movement of the active-region loops, the coronal propagating front ("EIT wave"), and the CME's leading edge strongly support the interpretation that all of these are aspects of an expanding volume. The evaluation in the context of two distinct MHD modeling efforts supports an interpretation in which a warming compression front moves significantly ahead of the erupting flux rope, at an interface between high active-region field, that all erupts with the rope, and the ambient field (likely rather potential in nature), with a current shell in between. Within the context of the MHD model discussed, this shell may have Joule dissipation within it at any time, but may take a few minutes to develop into a compression shell (by 01:53 UT, compare Table 1).

In the horizontal direction, the expansion is eventually limited to boundaries set by the enveloping volume of the helmet-streamer structure, so that when the front approaches a distance of about half a solar radius (depending on the direction), the moving front stalls (with some oscillatory response of the bounding field in the south) or simply fades away. The expansion at a height of 100 Mm or more above the surface is consistent with it occurring above the fields that connect AR 11158 to weaker regions to the north and northeast of it (compare Figures 5, 18, and 19). A faint perturbation seen moving toward and even over the north pole in the COR1 and COR2 images may be a wave that propagates after the expanding plasma volume that corresponds to the AIA observations of an "EIT wave" hits the boundaries of its magnetic volume (outlined by bright streamer stalks in *STEREO* observations).

Associated with the expansion of the erupting rope and the opening of the field is a ringing of the high coronal structures at the quiet-Sun to coronal-hole interface at the northern edge of the southern polar coronal hole. In the other three directions from the flare site, there is a very faint propagating feature high in the corona, which moves well beyond the edges of the coronal domain where the primary coronal propagating front stalls and fades, which we interpret as a compression of the plasma between the erupting volume and the surrounding streamer belts; such a compression might result in an EUV signal along the interface of open and closed field over a range of altitudes; we leave that for future study as we concentrate here on the much more obvious propagating front that is bounded by the footprint of the enveloping streamer.

Figure 22 illustrates the essential characteristics of our interpretation of the main propagating front for a simplified geometry.

8.2. Coronal Propagating Fronts in Broader Context

Our model-supported interpretation of the multi-perspective observations of the events early on 2011 February 15 suggests that the magnetic topology surrounding the eruption center is critical to the character of the phenomena that follow. Let us go through several scenarios. First, there is the possibility that an erupting flux rope (frequently with a well-defined filament at its core) does not make it into a full-fledged CME, but that its rise is halted at some height in the corona by constraints imposed by the surrounding field (examples of this are described by, e.g., Schrijver 2009). In such cases, one may envision an "EIT wave" to be initiated by the rapid rise and subsequent deceleration of the flux rope interacting with the overlying field; in such a scenario of a piston-driven wave, the possible "EIT wave" would have the aspects of magnetosonic or Alfvén-like waves, without a volumetric expansion beyond the confines of the closed magnetic configuration. It appears, however, that this scenario does not result in noticeable "EIT waves" as all such waves appear to be associated with CMEs (Delannée & Aulanier 1999; Biesecker et al. 2002). Perhaps this is because the "failed eruptions" slow down too gradually to excite a propagating wave.

If the eruption does manage to break through the high field of the source active region, the configuration of the large-scale field comes into play. If the domain of connectivity into which the eruption reaches next is confined to fairly low altitudes, then the expansion of this low-lying, relatively dense plasma environment is likely to be associated with a pronounced dimming, which is often seen in association with "EIT waves." In this scenario, phenomena associated with volumetric expansion would play a significant role, likely dominating over any wave-like attributes associated with the eruption and CME. Signatures of a magnetosonic wave may be found ahead of the compression front if the expansion is slow enough compared to the magnetosonic speed, or beyond the confines of the expansion (as we noted in faint signals northward of the streamer structure that bounds the CME's opening angle).

The details of the surrounding field likely affect how the eruption propagates. Both the opening angle over which the eruption extends and the direction into which it propagates relative to the radial direction can be determined by the field. One example of this is documented by Liu et al. (2010), who describe an eruption that extends into an opening angle projected on the solar surface of about 60°, propagating southward from an active region in the northern hemisphere's activity belt. These authors find evidence for both expansion and wave-like properties in the southward-propagating perturbation. Interestingly, a fan of relatively cool loops immediately to the north of the erupting region (and part of a northward-reaching domain of connectivity) shows no significant response to the large eruption adjacent to it, suggesting that any wave-like aspects of the eruption are highly anisotropic and travel in association with the expanding volume (compare, for example, the finding of markedly different lateral and radial expansions discussed by Veronig et al. 2010).

In the case of the 2011 February 15 eruption analyzed here, the eruption reaches into a high domain of connectivity almost immediately, causing the coronal propagating front to be weak

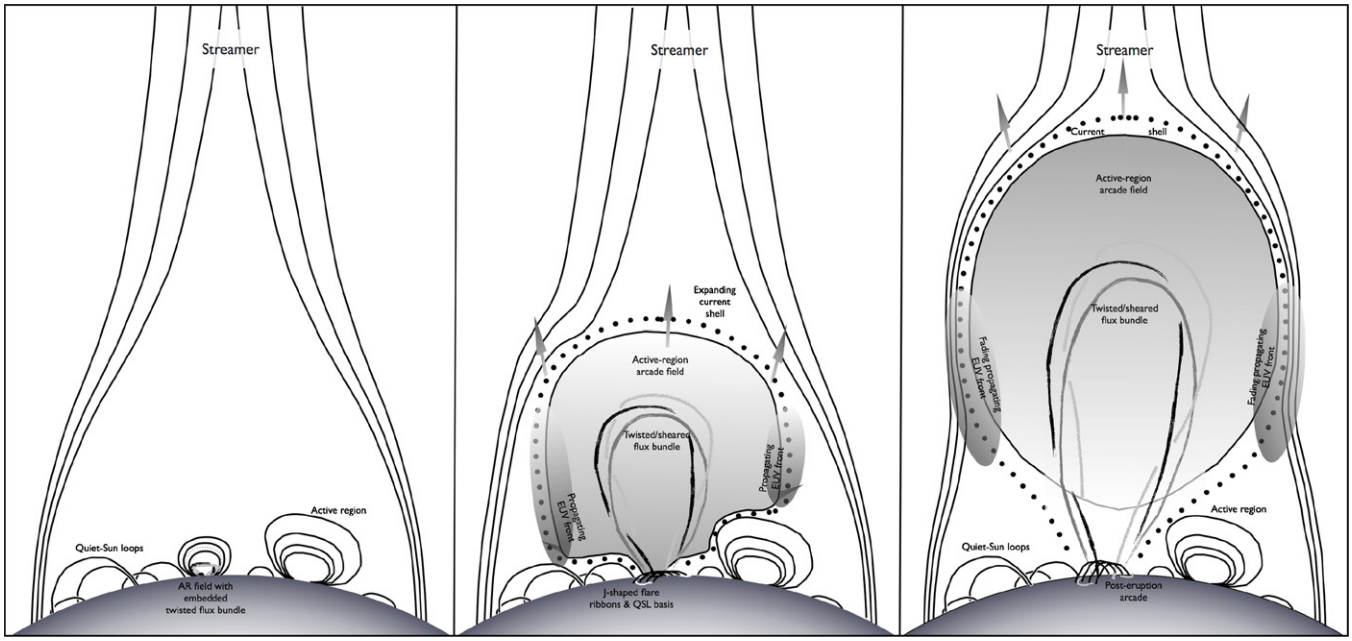

Figure 22. Sketch of the processes involved in a coronal propagating front as discussed in this study, rendered in a substantially simplified geometry that captures only the essential characteristics. On the left is a rendering of the pre-eruptive state: an active region with a sheared and twisted flux rope bundle, with a neighboring active region, both surrounded by a carpet of quiet-Sun field of a variety of lengths and strengths, underneath a cusp formed by closed field with field open into the heliosphere outside of it. In the center is a rendering with the eruption in progress: the shaded volume, containing the flux bundle and surrounding active-region field, is expanding rapidly, both in horizontal and vertical dimensions, affecting only the high regions of the strong-field environment of the active region. As the front moves up and out—visualized in the transition from the central to the right-hand panels—it distorts the boundaries of the coronal cusp, as it must in order to reach the heliosphere. The expansion front is compressing and warming the surrounding field and plasma at the enveloping current shell, resulting in the appearance of a propagating front (schematically indicated by the shaded ovals), which may manifest itself either as a brightening or as a dimming depending on the temperature of the plasma.

as it is a perturbation only on the high coronal emission, leaving the bulk of the emission that emanates from the corona beneath it unaffected (cf. Kienreich et al. 2009; Patsourakos & Vourlidas 2009). If the expansion is limited to the very high corona, no expanding front or coronal dimming may be see at all (as may be the case for the CME described by Robbrecht et al. 2009; see also Ma et al. 2010 on the statistics of "stealth CMEs").

The expansion of the 2011 February 15 eruption continues until it extends over the entire reach of a helmet-streamer oval, with at most weak wave-like perturbations extending beyond it visible only high in the corona (in the COR1 and COR2 images of *STEREO*). The bounding effects on CME extents by coronal topological domains defined by field connectivity that was noted for the eruption studied here (and as pointed out by Delannée et al. 2007 for a quasi-separatrix layer structure) raise the intriguing question whether this holds more generally. This would appear to be an interesting avenue of investigation as it might have direct impact on the modeling of coronal mass ejections and the forecasting of space weather.

The above considerations show the importance of global magnetic field modeling (at least in the potential-field source-surface approximation, if not the much more involved MHD modeling such as the work by Downs et al. 2011) in the study of how active-region eruptions manifest themselves in coronal and inner-heliospheric observations. They also emphasize that high-cadence, global, multi-spacecraft observations are crucial in the interpretation of observed phenomena.

This work was supported by the AIA contract NNG04EA00C to LMSAL. G.A. and E.P. were supported by the European Commission through the FP6 SOLAIRE Network (MTRN-CT-2006-035484). The MHD calculations were executed on the quadri-core bi-Xeon computers of the Cluster of the Division Informatique of Paris Observatory. We thank the referee for detailed comments and requests for clarification.

REFERENCES

Amari, T., Luciani, J. F., Aly, J. J., Mikic, Z., & Linker, J. 2003, ApJ, 595, 1231
Antiochos, S. K., Devore, C. R., & Klimchuk, J. A. 1999, ApJ, 510, 485
Aulanier, G., Golub, L., DeLuca, E. E., et al. 2007, Science, 318, 1588
Aulanier, G., Pariat, E., & Démoulin, P. 2005, A&A, 444, 961
Aulanier, G., Pariat, E., Démoulin, P., & Devore, C. R. 2006, Solar Phys., 238, 347
Aulanier, G., Török, T., Démoulin, P., & DeLuca, E. E. 2010, ApJ, 708, 314
Biesecker, D. A., Myers, D. C., Thompson, B. J., Hammer, D. M., & Vourlidas, A. 2002, ApJ, 569, 1009
Boerner, P., Edwards, C., Lemen, J. R., et al. 2011, Solar Phys., in press
Chandra, R., Schmieder, B., Aulanier, G., & Malherbe, J. M. 2009, Sol. Phys., 258, 53
Delannée, C., & Aulanier, G. 1999, Sol. Phys., 190, 107
Delannée, C., Hochedez, J.-F., & Aulanier, G. 2007, A&A, 465, 603
Delannée, C., Török, T., Aulanier, G., & Hochedez, J.-F. 2008, Sol. Phys., 247, 123
Démoulin, P., & Aulanier, G. 2010, ApJ, 718, 1388
Démoulin, P., Priest, E. R., & Lonie, D. P. 1996, J. Geophys. Res., 101, 7631
Downs, C., Roussev, I. I., van der Holst, B., et al. 2011, ApJ, 728, 2
Gallagher, P. T., & Long, D. M. 2010, Space Sci. Rev., 127
Howard, R. A., Moses, J. D., Vourlidas, A., et al. 2008, Space Sci. Rev., 136, 67
Hudson, H. S., Khan, J. I., Lemen, J. R., Nitta, N. V., & Uchida, Y. 2003, Sol. Phys., 212, 121
Kienreich, I. W., Temmer, M., & Veronig, A. M. 2009, ApJL, 703, L118
Kliem, B., & Török, T. 2006, Phys. Rev. Lett., 96, 255002
Kosovichev, A. G. 2011, arXiv:1102.3954
Lemen, J. R., Title, A. M., Akin, D. J., et al. 2010, Sol. Phys., in press
Li, H., Schmieder, B., Aulanier, G., & Berlicki, A. 2006, Sol. Phys., 237, 85
Liu, W., Nitta, N. V., Schrijver, C. J., Title, A. M., & Tarbell, T. D. 2010, ApJL, 723, L53

Ma, S., Attrill, G. D. R., Golub, L., & Lin, J. 2010, ApJ, 722, 289
Mackay, D. H., & van Ballegooijen, A. A. 2006, ApJ, 641, 577
Masson, S., Pariat, E., Aulanier, G., & Schrijver, C. J. 2009, ApJ, 700, 559
Moore, R. L., Sterling, A. C., Hudson, H. S., & Lemen, J. R. 2001, ApJ, 552, 833
Patsourakos, S., & Vourlidas, A. 2009, ApJL, 700, L182
Robbrecht, E., Patsourakos, S., & Vourlidas, A. 2009, ApJ, 701, 283
Schmieder, B., Aulanier, G., Demoulin, P., et al. 1997, A&A, 325, 1213
Schou, J., Scherrer, P. H., Bush, R. I., et al. 2011, Sol. Phys., in press
Schrijver, C. J. 2005, in Solar Wind 11/SOHO 16, Connecting Sun and Heliosphere, ed. B. Fleck, T. H. Zurbuchen, & H. Lacoste (ESA SP-592), 213
Schrijver, C. J. 2009, Adv. Space Res., 43, 739
Schrijver, C. J., & DeRosa, M. L. 2003, Sol. Phys., 212, 165
Schrijver, C. J., DeRosa, M. L., & Title, A. M. 2002, ApJ, 577, 1006
Schrijver, C. J., & Title, A. M. 2011, J. Geophys. Res., in press
Titov, V. S. 2007, ApJ, 660, 863
Ugarte-Urra, I., Warren, H. P., & Winebarger, A. R. 2007, ApJ, 662, 1293
van Ballegooijen, A. A., & Martens, P. C. H. 1989, ApJ, 343, 971
Veronig, A. M., Muhr, N., Kienreich, I. W., Temmer, M., & Vršnak, B. 2010, ApJL, 716, L57
Warmuth, A. 2010, Adv. Space Res., 45, 527
Wills-Davey, M., & Thompson, B. J. 1999, Sol. Phys., 190, 467
Zhukov, A. N. 2011, J. Atmos. Terr. Phys., 73, 1096